MASTERARBEIT | MASTER'S THESIS

Titel | Title

Colon and breast cancer spheroids: morphological characterization, formate overflow and transfectability with mRNA polyplexes

verfasst von | submitted by

Maja Stanic BSc

angestrebter akademischer Grad | in partial fulfilment of the requirements for the degree of

Magistra pharmaciae (Mag. pharm.)

Wien | Vienna, 2025

Studienkennzahl lt. Studienblatt | Degree programme code as it appears on the student record sheet:	UA 066 605
Studienrichtung lt. Studienblatt | Degree programme as it appears on the student record sheet:	Masterstudium Pharmazie
Betreut von | Supervisor:	Univ.-Prof. Dipl.-Ing. Dr. Manfred Ogris
Mitbetreut von | Co-Supervisor:	Haider Sami Ph.D.

Danksagung

Hiermit möchte ich mich herzlich bei Herrn Professor Manfred Ogris bedanken, dass ich meine Masterarbeit am „Laboratory of Macromolecular Cancer Therapeutics“ (MMCT) durchführen konnte. Während meiner praktischen Arbeit hatte ich das große Glück, in ein freundliches und unterstützendes Team aufgenommen zu werden.

Besonderer Dank gilt meinem Mitbetreuer Dr. Haider Sami für die stetige und kompetente Unterstützung, perfekte Betreuung, positive Art und bemerkenswerte Gelassenheit – selbst in stressigen Situationen.

Außerdem möchte ich mich bei Elisa Kulterer bedanken, da sie immer ein offenes Ohr für meine Fragen hatte und sich stets die Zeit genommen hat für mich - ganz gleich, ob es um die Arbeit oder unseren Meme-content ging.

Vielen Dank an alle MMCT-Kolleginnen und Kollegen für die freundschaftliche und positive Atmosphäre - und ganz besonders für die unterhaltsamen und aufheiternden Gespräche in den Mittagspausen, die den Arbeitsalltag angenehmer gemacht haben.

Mein besonderer Dank gilt auch Nina Neunteufel für ihre Unterstützung sowie Ermutigung jeglicher Art während dieser Masterarbeit. Ohne sie wäre diese Zeit nur halb so wertvoll gewesen.

Ein herzliches Dankeschön geht an meine Familie, die mich immer sowohl finanziell als auch mental unterstützt hat, und für ihre Geduld, wenn ich mich manchmal tagelang oder wochenlang nicht gemeldet habe.

Ein liebes Danke gilt auch meinem Freund Ivan Jovanovic, der mich stets versucht hat zu verstehen und immer den Rücken gestärkt hat, vor allem jetzt in der Endphase.

Abschließend möchte ich mich bei allen Freunden bedanken, die in irgendeiner Weise zum Entstehen dieser Arbeit beigetragen haben – sei es durch motivierende Worte oder einfach durch ihr Verständnis für meine zeitliche Abwesenheit während der intensiven Arbeit- und Schreibphasen.

Vielen Dank!

Table of Contents

1 Abstract

Since cancer is considered an emerging disease, more promising and innovative therapy approaches are needed to provide effective treatment options. Especially, understanding and identifying the driving cause is an important key factor in oncological research. This thesis focuses on 3D cancer spheroid models, which are an essential tool to gain insights in cancer pathophysiology and mimic tumor-like environment. For this objective, spheroids based on either murine colon cancer or breast cancer cells were employed. Their morphology, like necrotic core establishment, was studied. The production of formate, a metabolic byproduct, was quantified as well as their transfectability with various polyplexes.

In case of colon cancer spheroids, CT26Luc cells were seeded at different numbers to form compact spheroids, and their morphology was observed via phase contrast microscopy. The formation of the spheroid´s necrotic core was evident after two to three days and visualized after staining employing propidium iodide via fluorescence microscopy. Additionally, formate production was successfully measured using a colorimetric assay. The effect of oxaliplatin treatment on CT26Luc spheroids at various concentrations and with different incubation times was assessed, indicating that the timing of administration holds an important role in treatment efficiency. Transfection experiments revealed that CT26Luc spheroids could be successfully transfected with luciferase encoding plasmid using linear polyethyleneimine.

Breast cancer spheroids were formed with murine 4T1 triple negative breast cancer cell line exhibiting a stable knockdown of methylenetetrahydrofolate dehydrogenase (4T1-MTHFD1L), a mitochondrial enzyme responsible for formate production, and compared with spheroids from control cell line 4T1 SCR. For both cell lines, formate concentration was assessed on designated days. Phase contrast microscopy and necrotic core staining demonstrated clear differences between the morphology of the two breast cancer cell lines, highlighting the role of formate in tumor behaviour and structural organization. 4T1 SCR spheroids were then tested for transfection with mRNA and plasmid-based polyplexes. Here, polyplex formulation had a greater impact on transfection efficiency rather than the period of spheroid growth ranging from day 8 to day 15 after seeding.

2 Zusammenfassung

Da Krebs zu den emergierenden Krankheiten gehört, sind bessere und innovative Therapieansätze erforderlich. Diese Arbeit konzentriert sich auf 3D-Krebs-Sphäroid-Modelle, die wesentliche Einblicke in die Krebs-Pathophysiologie liefern und tumorähnliche Umgebungen imitieren. Zu diesem Zweck wurden Sphäroide von murinen Dickdarmkrebs- und Brustkrebszellen verwendet. Sie wurden auf ihre Morphologie, die Bildung des nekrotischen Kerns und die Produktion von Formiat, welches ein Nebenprodukt des Stoffwechsels ist, untersucht. Ebenso wurde die Transfektibilität mit verschiedenen Polyplexen analysiert.

Für die Darmkrebs-Sphäroide wurden aus murine CT26Luc-Zellen kompakten Sphäroiden gebildet und ihre Morphologie mittels Phasenkontrastmikroskopie analysiert. Die Bildung des nekrotischen Kerns der Sphäroide war nach zwei bis drei Tagen erkennbar und wurde durch Fluoreszenzmikroskopie mittels Propidiumjodid visualisiert. Darüber hinaus wurde auch die Formiat-Produktion mit einem kolorimetrischen Assay gemessen. Die Wirkung von Oxaliplatin auf CT26Luc-Sphäroide wurde bei verschiedenen Konzentrationen und Inkubationszeiten untersucht, was die Bedeutung des Verabreichungszeitpunkts für die Behandlungseffizienz unterstreicht. Transfektion-Experimente zeigten, dass CT26Luc-Sphäroide mittels linearem Polyethylenimin erfolgreich mit Luziferase-kodierendem Plasmid transfiziert werden konnten.

Brustkrebs-Sphäroide wurden mit der murinen 4T1-Zelllinie gebildet, bei der die Methylentetrahydrofolat-Dehydrogenase (4T1-MTHFD1L), ein mitochondriales Enzym, welches für die Formiat-Produktion verantwortlich ist, stabil ausgeschaltet war, und mit Sphäroiden der Kontrollzelllinie 4T1 SCR verglichen. Für beide Zelllinien wurde die Formiat-Produktion an bestimmten Tagen gemessen. Die Phasenkontrastmikroskopie und die Färbung des nekrotischen Kerns zeigten deutliche Unterschiede zwischen den Sphäroiden der beiden Zelllinien, was die Rolle des Formiats für das Tumorverhalten und die strukturelle Organisation verdeutlicht. Die 4T1-SCR-Sphäroide wurden anschließend für die Transfektion mit mRNA und Plasmid-basierten Polyplexen getestet. Hier hatte die Formulierung des Polyplexes einen größeren Einfluss auf die Transfektionseffizienz als die vorhergehende Dauer des Sphäroidwachstums.

3 Abbreviation

AMPK	AMP-activated protein kinase
MTHR	Methylenetetrahydrofolate reductase
SHMT1/2	Serine hydroxy methyltransferase 1/2
MTHFD1/2	Methylenetetrahydrofolate dehydrogenase 1/2
MTHFD1L	Methylenetetrahydrofolate dehydrogenase (NADP+ dependent) 1-like
THF	Tetrahydrofolate
TYMS	Thymidylate synthetase
CRC	Colorectal cancer
CIN	Chromosomal instability
APC	Activated protein C
KRAS	Kirsten rat sarcoma virus
PIK3CA	Phosphatidylinositol-4,5-bisphosphate 3-kinase catalytic subunit alpha
BRAF	V-Raf murine sarcoma viral oncogene homolog B
SMAD4	Mothers against decapentaplegic homolog 4
MSI	Microsatellite instability
MMR	Mismatch repair
CIMP	CpG island methylation pathway
MLH1	MutL protein homolog 1
BRCA1/2	Breast cancer gene 1/2
ER	Estrogen receptor
PR	Progesterone receptor
HER2	Human epidermal growth factor receptor 2
TNBC	Triple negative breast cancer
ECM	Extracellular matrix
TME	Tumor microenvironment
MCT	Multicellular tumor
OCT	Optical coherence tomography

FLM	Fluorescent microscopy
PI	Propidium iodide
NP	Nanoparticles
PEI	Polyethyleneimine
LPEI	linear PEI
cLPEI	crosslinked LPEI
BPEI	branched PEI
GFP	Green fluorescent protein
GLuc	Gaussia luciferase
RSZ	Resazurin
MTT	3-[4,5-dimethylthiazol-2-yl]-2,5 diphenyl tetrazolium bromide
pDNA	Plasmid DNA
mRNA	Messenger RNA
SCR	Scrambled
PBS	Dulbecco's phosphate buffered saline
HBG	HEPES buffered glucose solution
RFU	Relative fluorescence unit
RLU	Relative luminescence unit

4 Introduction

4.1 Cancer: role of formate

According to the World Health Organization (WHO), one in five people develop cancer in their lifetime. The commonly occurring cancer type leading to death is lung cancer, followed by female breast cancer and colorectal cancer. By 2050, it is estimated that 30 million new cancer cases will be diagnosed. This increase is attributed to population ageing and growth, as well as greater exposure to various risk factors, such as tobacco use, alcohol consumption and obesity[1].

Cancer is a group of diseases characterized by their complexity of multiple distinct cell types. In addition to cancer cells, normal cells are also recruited to form the tumor-associated stroma, additionally known as the tumor microenvironment. The heterogeneity of the cancer tissue involves several key traits, including chronic proliferation, evasion of growth suppressors, resistance to cell death, induction of angiogenesis, avoiding immune destruction, deregulation of cellular metabolism replicative immortality and activation of invasion and metastasis. These collected traits are referred to as the hallmarks of cancer. While normal tissue maintains a balance between growth-promoting and supressing signals, tumor cells are able to deregulate these signals, resulting in uncontrolled growth and invasion of surrounding tissues. Additionally, two key factors were identified, which accelerate tumor progression. The first is genomic instability, which leads to an accumulation of random mutations. The second key factor involves the induction of inflammatory conditions in premalignant and malignant lesions, driven by the immune system and leading to negative outcomes, resulting in manifestation of the cancer hallmarks. Together, these factors enable neoplastic diversity, making cancer difficult to treat as tailored therapies must be developed for each case[2].

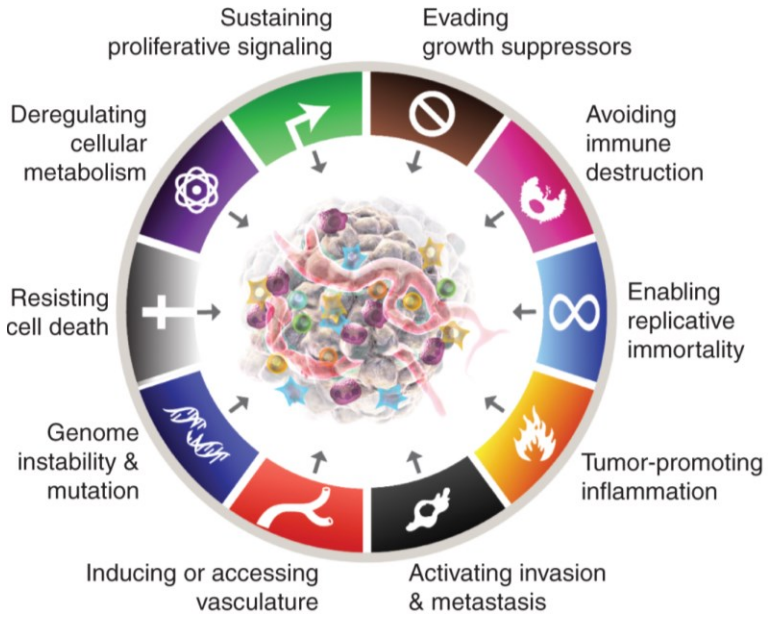

Figure 1: The hallmarks of cancer development: A simple overview of the eight underlying key traits as well as the newly identified key factors for cancer progression. Adapted and modified form Hanahan et al[2].

The recognition of deregulated cellular metabolism and metabolic reprogramming as a hallmark of cancer is a relatively new advancement. These alterations happening on cellular level enable cancer cells to dynamically adjust their metabolic activities to favour proliferation and survival. In addition to this, normal cells possess the ability to sense metabolic changes, triggering a cascade of reactions referred to as metabolite sensing. Cancer cells exploit this way of communication, utilizing their altered activity to regulate the types and concentrations of metabolites within the tumor microenvironment. This sensing mechanism leads to regulation of signalling transduction pathways and drives epigenetic modifications. Metabolite sensing is crucial for the cancer cells to communicate with their external environment, reprogramming it to their advantage. This adaptive capability significantly contributes to therapy resistance and invasion in normal tissue[3].

Cancer cells rely on both the recruitment of various cell types for the tumor microenvironment and the acquisition of specific macromolecules to sustain and grow. The tumor depends on the surrounding stroma to obtain essential nutrients, while also using intracellular anabolic pathways to generate additional required components. Respectively, pathways regulating increased flux through glycolysis, the tricarboxylic

acid cycle, and one-carbon metabolism are often dysregulated in cancer cells. These pathways are essential for the nucleotide-production and haem synthesis, both are crucial for cancer progression. Tumors harbour a vast metabolic complexity, which is not yet fully understood. Further research is needed to identify novel metabolic pathways and the intermediate products used by cancer cells during tumor initiation, progression and metastasis[4].

A key intermediate metabolite that has attracted attention is formate. Formate is part of the one-carbon (1C) metabolism, which plays an essential role in the cellular and systemic metabolism of mammals. One-carbon metabolism encompasses a vast number of biochemical reactions involving the utilization, transfer or production of 1C units, either as free molecules or attached to carrier compounds. This pathway can be subdivided into different branches depending on the specific co-factors involved. The co-factors are either folate dependent or folate-independent, with the latter being linked to formaldehyde metabolism. The folate dependent pathway represents the core of 1C metabolism, where formate is majorly derived from serine. This metabolic reaction primarily takes places in the mitochondria. In this context, formate is essential for the biosynthesis of nucleotides and also interacts with energy metabolism. Given its crucial functions, it is unsurprising that alterations or dysregulation of formate production are linked to various human diseases such as cancer [5].

Mammalian cells typically generate formate at excessive rates exceeding the biosynthetic needs. Excessive formate is then released from the cells, a phenomenon known as formate overflow. Both folate-dependent and folate-independent pathways are capable of meeting the one-carbon demand for cell proliferation. However, the folate-dependent mitochondrial pathway is primarily responsible for formate overflow. Cancer cells often exhibit dysregulated mitochondrial formate production, resulting in increased formate levels. The increase of formate induces a metabolic switch, enhancing purine and pyrimidine production as well as boosting energy metabolism. Latter is partly due to repressed AMPK activity. These changes have been associated with cancer progression and metastasis. Mice fed a diet low in serine displayed delays in tumor growth highly contributed to deprivation of this key precursor in one-carbon metabolism. However,

further work is required to identify the exact role of formate and formate-induced switch in cancer pathophysiology[6].

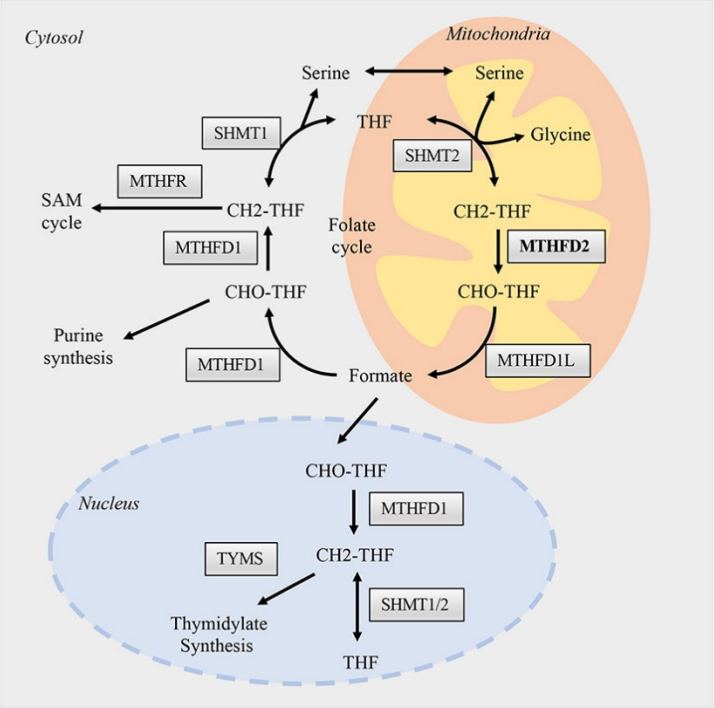

Figure 2: The role of formate in the one-carbon metabolism: Formate serves as a transferable one- carbon unit inside the cells which is able to permeate between the compartments. It can then be further biosynthesized to purine and thymidylate in the cytosol and nucleus respectively. The main responsible enzymes are presented. Figure form Zhu et al[6].

4.1.1 Colon cancer

Colorectal cancer (CRC) ranks among the most commonly diagnosed cancers after lung and breast cancer. Advances in screening, detection of risk factors and treatment have led to a decrease in CRC incidence among patents over 50 years. However, epidemiological studies show an alarming rise in CRC cases among individuals under 50 years of age. Approximately 10 % of all new CRC diagnoses are attributable to early-onset CRC. Typically, the risk of getting CRC is assessed based on age and family history. Surprisingly, in the United States, 3 out of 4 patients with early-onset CRC report no family history of the disease. Similar data has been collected internationally, including Canada, Australia, the United Kingdom and Asia. Notably, identified risk factors for CRC in older

patients seem to play a reduced role in younger individuals. Moreover, the exact mechanisms and contributing causing early-onset CRC remain poorly understood [7].

CRC encompasses both colon and rectal cancer, which share similarities in biological basis. However, the diagnostic approaches and treatments strategies differ in both. Colon cancer often appears sporadically with risk factors including age, race, lifestyle and inflammatory bowel disease. Hereditary forms of colon cancer account for approximately 5 % of newly diagnosed cases and are attributed to inherited genetic mutations such as those associated with Lynch syndrome and familial adenomatous polyposis[8].

On a molecular level at least three major pathways are responsible for the development of colon cancer, with chromosomal instability (CIN) being the most prevalent. CIN involves chromosomal abnormalities, including structural changes and varying chromosome numbers. These alterations are linked to mutations in key genes like APC, KRAS, PIK3CA, BRAF, SMAD4 and p53. All of these genes play a crucial role in cell proliferation and the cell cycle regulation, ultimately driving cancer development and progression[9].Another pathway involved is the microsatellite instability (MSI), characterized the dysfunction of the DNA mismatch repair (MMR) genes and thus resulting in hypermutability. The third pathway linked to tumorigenesis is the CpG island methylation pathway (CIMP, which is associated with abnormal DNA methylation patterns. Colon cancers categorized as CIMP+ can be further divided into two subtypes: $CIMP^{high}$ tumors, which are linked to BRAF mutations and MLH1 methylation, and $CIMP^{low}$ tumors, related to KRAS mutations. Often, cancer development arises from a combination of all these pathways[10].

To gain a better understanding of the tumorigenesis and to improve preclinical evaluation in drug discovery, murine colon cancer models were established. Among the most heavily used and oldest preclinical models are syngeneic tumor cell lines, which derived from inbred strains of mice. In these models, cancer cells – either spontaneous, carcinogen-induced or transgenic – are isolated and thus can be further expanded in vitro. The isolated cancer cells then are implanted into immunocompetent mice which descend from the same strain and tumor growth can be monitored in an in-vivo setting [11].

One commonly used cancer cell line is CT26, which derived from colon cancer in weakly immunogenic BALB/c mice. To enhance imaging of the CT26 cells, they were transduced with a retrovirus vector, which stably expresses the firefly luciferase gene. This modification led to the creation of the CT26Luc cell line. The expression of luciferase allows better tracking and visualization of the cancer cells in experimental settings.[12]

4.1.2 Breast cancer

In 2022, breast cancer was the most common cancer in women in the majority of countries globally, accounting of around 670 000 deaths worldwide. According to the WHO, breast cancer predominantly occurs in women with an incidence rate of about 1 % of all newly diagnosed cases [13].

The clear cause of breast cancer manifestation remains poorly understood. Hereditary factors amount to only 5-10 % of all breast cancer cases, with germline mutations in BRCA1 or BRCA2 contributing to roughly 30 % of all inherited incidences. Identified risk factors include early menarche, later menopause, hormone intake, lifestyle, age, obesity, alcohol and tobacco consumption. Additionally, environmental exposures, such as chemicals and radiation have also been linked to increased breast cancer incidences. Despite advancements in breast cancer treatment in the last years, successful prevention of the disease is still outstanding. The clear cause is still shrouded in uncertainty respectively to what triggers or influences breast cancer development[14].

Breast cancer is a very heterogenous disease, caused by a variety of genetic alterations and thus leading to different disease manifestations in individuals. As a result, breast cancer was the first human cancer whose treatment approach was customised based on molecular characteristics found in patients individually. Breast cancer can be classified based on the presence of three key receptors: estrogen receptor (ER), progesterone receptor (PR) and human epidermal growth factor receptor 2 (HER2). There are also tumors in which none of these receptors are present (triple-negative). These classes can be further subdivided into distinct molecular subtypes. The identified subtypes are the basis for treatment decisions and therapy. Due to the dynamic character of the breast cancer cells, there is even a possibility for a dynamic interconversion between the

different molecular subtypes. Both the malignant epithelium and the tumor microenvironment play a key role in the heterogeneity. This heterogeneity has to be considered when selecting specific anti-cancer therapy, as failure to do so can lead to resistance and treatment failure[15].

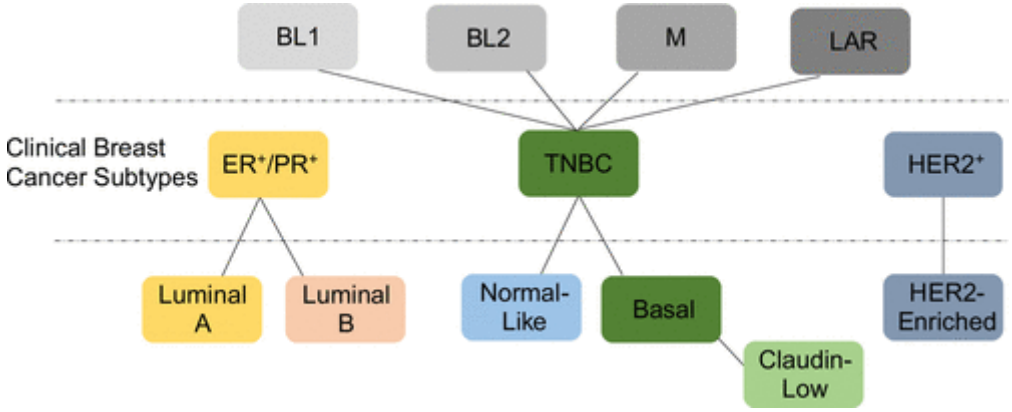

Figure 3: Classification schema based on molecular status for breast cancer. The presence of the three key receptors ER, PR, HER2 and absence of all three (TNBC) can be further subdivided by their gene signature via prediction analysis of microarray 50 (PAM50) into five distinct subtypes shown in the lower half of the figure. The basal subtype can be further classified into claudin-low subtype. TBNC can, in parallel, be organized into four distinct subtypes: basal-like 1 (BL1), basal-like 2(BL2), mesenchymal (M) and luminal androgen receptor (LAR). ER=estrogen receptor; PR=progesterone receptor; HER2= human epidermal growth factor receptor 2; TBNC=triple negative breast cancer. Figure from Turner et al[15].

Among the different subtypes of breast cancer, the triple negative breast cancer (TNBC) is known for its aggressive nature in tumor progression, metastasis and reoccurrence[16].

To gain a better understanding of the pathophysiology of breast cancer, mouse models are widely used in research. One prominent example is the 4T1 murine breast cancer cell line, which are isolated from BALB/c mice. 4T1 models closely mimic the tumorigenesis due to their similar characteristics to advanced TNBC human mammary carcinoma. Their highly tumorigenic nature and ability to form progressive metastasis in multiple distant tissues make them an invaluable setting for studying breast cancer development and treatment approaches in preclinical settings[17].

Since cancer metastasis plays a crucial role in the survival of patients and anti-tumor treatments are mostly ineffective in advanced stages, understanding the cancer

pathophysiology and preventing metastasis is important. The key role of one-carbon metabolism in tumorigenesis and metastasis suggests connections that could pave the way for new treatment approaches. By targeting metabolic pathways such as one-carbon metabolism, cancer survival, growth and spread may be disrupted. In the 4T1 mouse model, knocking down the MTHFD1L gene had an impact on metastasis progression, but not on tumor growth itself. This gene is linked to the tumor´s need for three key resources: biomass, redox equivalents against oxidative stress, and bioenergy generation. All three hallmarks are needed for survival. During metastasis, cancer cells need to adjust their metabolism, a process called serine plasticity. This metabolic rewiring enables the tumor to meet the growing demands for either building blocks (biomass) or energy. Biomass is mainly produced in the cytosol, while redox equivalents and bioenergy are generated in mitochondria, the latter two are due to excessive formate overflow. These elevated formate levels in the tumor microenvironment are suspected to enhance cancer invasiveness, driving metastasis. MTHFD1L is an enzyme mostly expressed in mitochondria and responsible for degrading serine to formate. When the expression of the enzyme is reduced, the mitochondrial one-carbon metabolism is impaired, leading to limited formate production. While knocked out MTHFD1L did not reduce the tumor growth, it certainly did have a positive effect on motility and migration of the tumor. This research highlights the potential of targeting metabolic vulnerability for new treatment approaches[18].

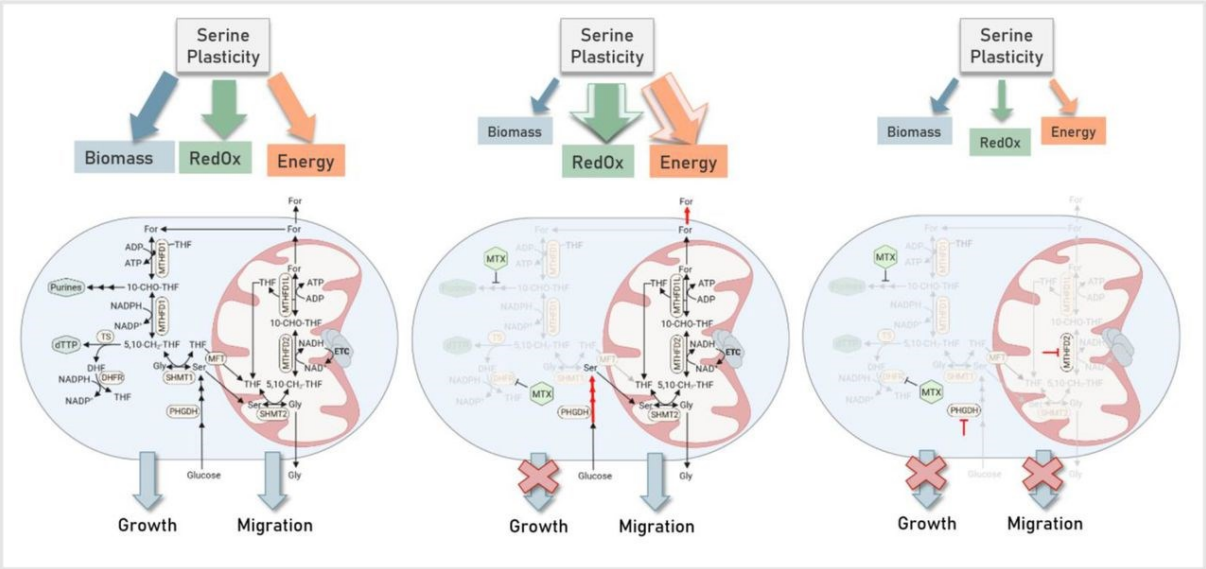

Figure 4: Overview of the shifting serine plasticity and their outcome for cancer progression: In cancer cells serine is the main source for biomass, redox equivalents and bioenergy production. With methotrexate (MTX) treatment, a commonly used cancer treatment, biomass production can be intermitted. However, this leads to the cancer cells rewiring their metabolic pathways to high serine catabolism in the mitochondria. As a result, formate production via the one-carbon metabolism is increased and excessive formate is released extracellular. This formate overflow in the tumor microenvironment is suspected to be partly responsible for cancer invasiveness and metastasis. The downregulation of the MTHFD1L enzyme shows decreased metastasis formation. Figure from Kiweler et al[18].

4.2 Three-dimensional cell culture models

Despite their establishment in research, animal studies entail certain disadvantages such as ethical concerns, caretaking and handling of the animals as well as the challenges in translating findings to human application. Therefore, cell culture models play a central role in oncology research yet come with their own set of constraints. The traditionally used two-dimensional (2D) cell cultures fail to represent the physiological human setting, particularly in mimicking the tumor microenvironment. Respectively, cancer is characterized by its inherent complexity, involving cell-cell and cell-matrix interactions, which are difficult to recreate in conventional 2D systems[19].

To address these limitations, three-dimensional (3D) cell culture models were established. One of the biggest advantages lies in their ability to recreate a biological "microsetting" in-vitro, closely mimicking the morphology, promoting cell proliferation and driving heterogeneity of the tissue. 3D models bridge the gap between simple monolayer cell cultures and the gold standard, in vivo animal studies. 3D models

represent a more accurate version of tumor characteristics and lead to clearer observation. Additionally, nowadays a wide range of 3D models and systems is available, each having its own strength and applications [20].

4.2.1 Different approaches to forming 3D cell culture models

3D cell culture models can be categorized into various types based on their method of preparation and final organisation. Among these, scaffold-based models are one of the most commonly used methods. The scaffold acts as a structural framework, supporting growth and organization of the cancer cells. They can be made from synthetic, natural or mixed components and serve as surface for the cancer cells to grow. Once the cancer cells are attached onto the scaffold, they start to proliferate and eventually degrade the scaffold while forming their own extracellular matrix (ECM). To achieve desired 3D cell culture outcome scaffold properties – such as porosity, surface chemistry and many more – can be adjusted[21].

Another approach to forming 3D cell culture is via liquid-based culture systems. The hallmark of this method is the prevention of cell adherence to the bottom of the culture vessel, forcing cancer cells to attach to themselves. This can be achieved through either coating the surface, gravity or maintaining a dynamic fluid flow so that cells are not able to settle on the bottom (Figure 5). The formed cell aggregate, known as spheroids, are able to mimic the chemical and physical gradient characteristics of tumor tissue. The easiest way to form spheroids is by seeding cancer cells in low-attachment plates. Another straightforward technique is the hanging drop culture method, where cancer cells are suspended in a small droplet of media which is inversely hanging form the lid of a non-coated culture dish, relaying on gravity and surface tension. Additionally, spheroid formation can be formed in a setting with continuous agitation, which increases collisions between cells and prevents the attachment on the surface. This continuous fluid flow can be maintained by stirring and keeping bioreactors or culture bottle in constant movement[22].

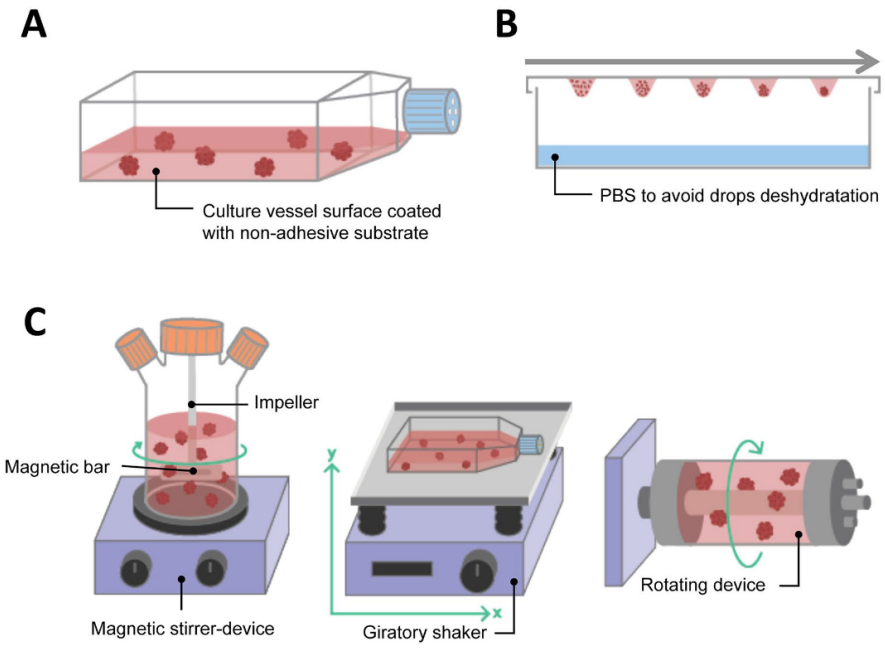

Figure 5: An overview of different methods to form 3D cell culture in liquid-base culture systems. A) Displays the method of seeding cells in a flask (same principle for well plates) with non-adhesive coating. B) Illustrates the hanging drop technique. C) Shows the different devices to achieve a continuous agitation in the culture vessel forcing the formation of cell spheroids. Adapted and modified from Jubelin et al[22].

Emerging methods for 3D tumor models include organoids and bioprinting, representing future prospectives in mimicking the biological environments of malignant tumors. Organoid technology utilizes samples derived either from patient biopsies or genetically engineered wild types. Patient-derived cancer organoids retain the individual heterogeneity, making them valuable systems for personalized treatment development[23]. Bioprinting stands out as the most progressive method among 3D cell culture systems. Its principle encompasses cell culture as "bioink" which is embedded within a customized matrix, enabling a layer-by-layer assembling of tissue-like structures in a controlled space and organization. Bioprinting enables the production of complex tissues with tailored properties, which could play a key role in in-vitro disease modelling and deeper insights of individual tumorigenesis[24].

4.2.2 Cell spheroids

This abstract emphasizes the properties, usage, advantages and limitations of spheroids in in-vitro cancer research.

Spheroids with diameters extending 500 µm show similarities to solid in-vivo tumors ranging in size from 0,5 to 1 mm^3. These 3D cell cultures mimic tumor-like properties, offering better insights to the cancer cells behaviour and treatment responses. A key feature involves the development of hypoxia, due to increased oxygen diffusion distances in growing spheroids. The outer layers of the spheroid have a better access to oxygen compared to the core, resulting in an established oxygen gradient. To counteract hypoxia, cancer cells undergo a metabolic shift towards anaerobic degradation of glucose, leading to an elevated production of lactate – also known as Warburg effect. The increased production of lactate induces an acidic milieu, comparably to the conditions in solid tumors. Additionally, the lack of oxygen drives the upregulation of hypoxia-inducible family (HIF) factors and increased expressions of multidrug resistance gene. Furthermore, nutrient deprivation and the metabolic shift can result to cell cycle arrest, leading to a dormant state that renders cancer cells less susceptible to canonical anti-cancer therapeutics. Moreover, spheroids also exhibit altered cell-cell interactions, such as increased E-cadherin expression. This enhances cancer cell survival and is similarly observed in solid tumors. In addition, the tumor microenvironment (TME) is crucial in treatment success in cancer. Similarly, spheroids display an abnormal extracellular matrix (ECM), closely imitating the altered cell-matrix interactions of their in-vivo counterparts[25].

Spheroids can be produced by different methods, as described previously. However, the effectiveness of the in-vitro models depends crucially on the type and mixture of cells used. Spheroids can be formed either using monocellular cancer cell lines - genetically modified or wild type - or heterocellular cancer cells, with or without scaffolds. The differences among these spheroids lie in their cell source, complexity and application in research. For instance, mono-multicellular tumor (MCT) spheroids are commonly used for studying cancer cell behaviour, morphological and physiological characteristics. While hetero-MCTs consist of multiple cell types, including components of the ECM. The present complexity makes hetero-MCTs valuable models for investigating tumor heterogeneity, tumorigenesis and assessing the efficacy of new therapeutic drugs[26]. Figure 6 illustrates the advantages and limitations of different MCTS models.

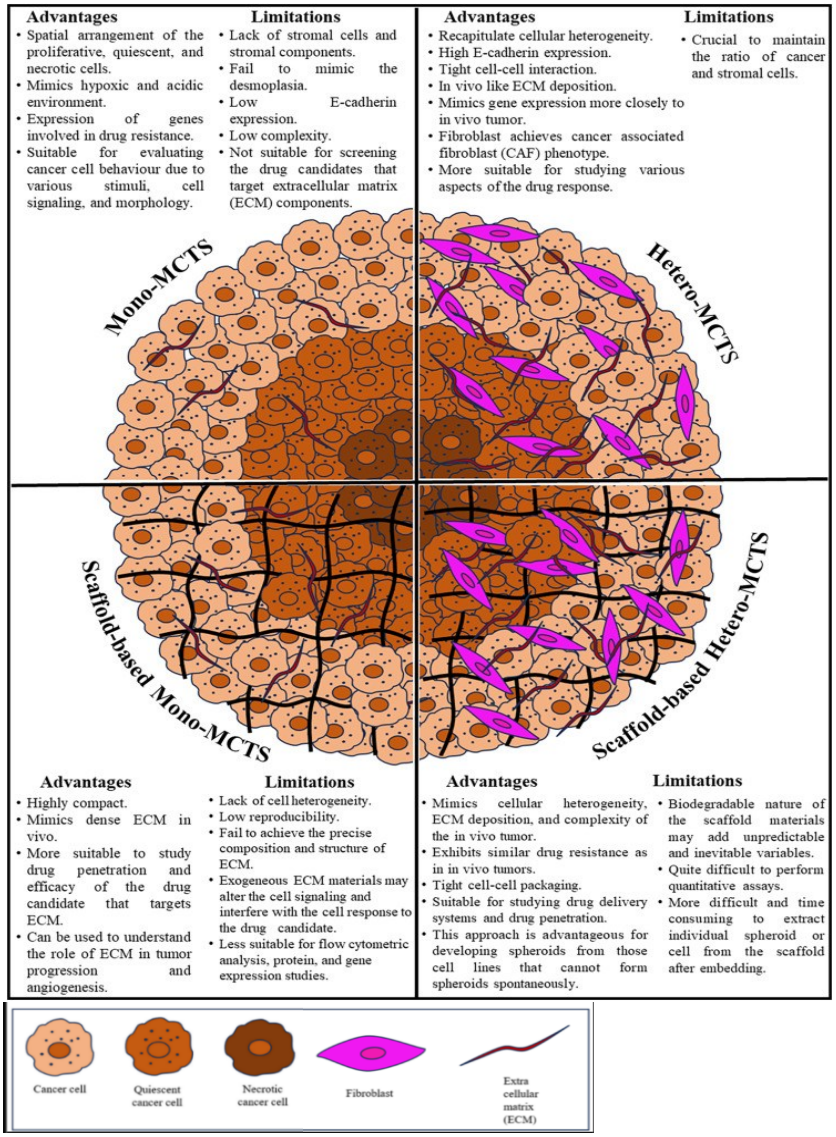

Figure 6: An overview of the advantages and limitations of mono and hetero-multicellular tumor systems (MCTS). Adapted and modified from Patel et al[26].

Limitations of 3D spheroid models

One of the primary limitations of 3D cell culture models is the instability of the produced TME, particularly regarding the acting immune cells. Immune cells are difficult to keep in-vitro settings because they require specific conditions to sustain their viability and functionality. Furthermore, the individual TME of the patient is not fully reproduceable, as the T-cells composition vary between individuals. Additionally, allogenic reactions may occur, producing misleading data. Despite these challenges, 3D cell culture models play a crucial role in studying certain tumor characteristics and deepening the insights of cancer biology[27].

4.2.3 Spheroid growth

The spheroid formation process is divided into three steps, as shown in Figure 7b. Initially, ECM proteins facilitate the rapid assembly of the cancer cells to lose aggregates through integrin binding. This is followed by a delay phase, in which cadherins are expressed and accumulated. Finally, upregulated E-cadherin expression and homophilic interactions result in the formation of compact spheroids[28].

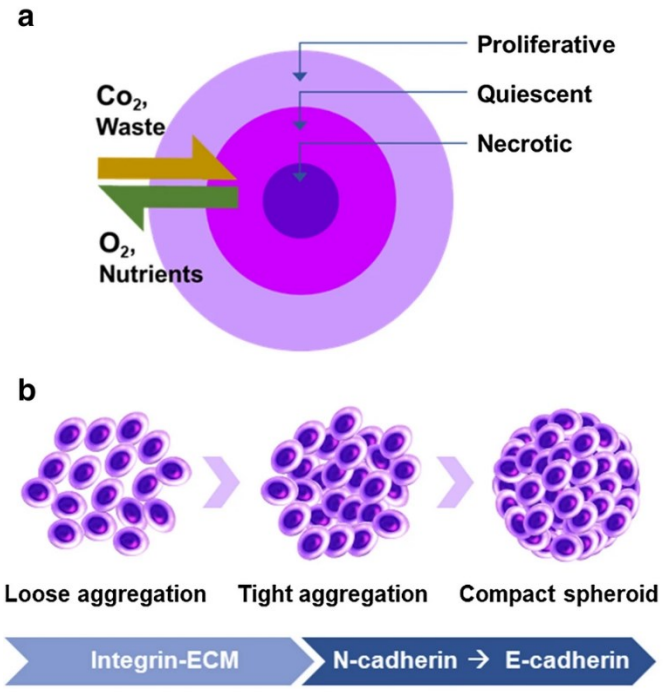

Figure 7: Structural organization and formation of multicellular tumor (MCT) models: a) The MCT is divided into three layers, starting with the proliferative layer on the outside, the quiescent layer in the middle and the necrotic core within the spheroid. This distinction is mainly happening because physical gradients (oxygen, carbon dioxide and nutrients) are established. b) The formation of spheroids begins with a loose aggregation of the cancer cells. Over the time these aggregations tighten through N-cadherin and later E-cadherin expression and interactions. Adapted and modified from Han et al[29].

Once seeded, spheroids need some time to form and mature. Spheroids beyond 500 µm in size begin to mimic avascular in-vivo tumors, characterized by different heterogeneous layers. The outer layer consists of proliferating cancer cells, the middle layer contains quiescent and dormant cells, and the spheroid core develops a necrotic region due to apoptosis. These layers arise from the previously described physical gradients, such as

limited oxygen and nutrients diffusion towards the centre. The final morphology and structure depend on the cancer line and method used for formation. For instance, in scaffold-free systems cells with higher expression of adhesion molecules like E-cadherin form more compact spheroids, while those with lower expression form looser cell aggregates. In cases, where adhesion molecules are insufficient, spheroids cannot be formed without additives or scaffold-based systems[29].

Furthermore, the formation method used crucially influences the spheroids characteristics, including growth-induced solid stress, surface topography and stiffness. Newly seeded spheroids, even with comparable cell density, often exhibit flatter shapes, whereas rounder and more spherical structures start to form after a few days, as growth-induced stress accumulates. This accumulation and altered surface properties are closely linked to responses to anti-cancer treatments. Thus, resulting in differences in drug permeability within the spheroid and, in some cases, creating a distinct barrier that hinders effective drug diffusion[30].

4.2.4 Necrotic core visualization

Recent hypotheses suggest that factors secreted by necrotic regions may induce cancer progression and impact treatment outcomes negatively. Prolonged exposure of cells to metabolic stress and hypoxia has shown to activate specific intracellular pathways, driving cancer formation to a more aggressive tumor phenotype. This adaption not only contributes to tumor progression but also increases the likelihood of developing resistance to therapeutic interventions[31].

The characterization of the necrotic core in-vitro can be achieved with gold standard modalities like histological staining or fluorescent staining. Histological staining involves fixing, embedding and slicing of spheroids into thin sections (approximately 5-10 µm). These sections then can be stained with either traditional dyes like hematoxylin and eosin or through immunochemical stainings. These methods, however, are invasive and only bring forth 2D perspectives of the necrotic core within the spheroids. Fluorescent imaging, on the other hand, enables visualization of the necrotic core in a 3D setting and is described in detail below. Emerging modalities such as optical coherence tomography

(OCT) represent an imaging technique where 3D images are obtained label free and in a non-destructive manner. Thus OTC enables continuous monitoring of the spheroids over time without causing any structural damage [32–34].

Fluorescent microscopy imaging (FLM) is commonly utilized to assess viable and dead cells in the spheroids, as well as their distribution throughout the 3D structure. By applying fluorescent dyes, which penetrate the spheroid over time via a formed gradient, FLM allows the visualization of the accumulated dyes in the cancer cells, either through generating 2D images of the spheroid structure or 3D reconstructions via Z-stacks. The uptake of dye in the cancer cells depends on the different properties of the used substances. For example, Hoechst (excitation/emission = 350/461 nm) is a fluorescent dye that stains the nuclei of viable cells blue. Propidium iodide (PI, excitation/emission = 538/617 nm), on the other hand, selectively accumulates in apoptotic and necrotic cells, staining them yellow[35]. A combinational staining of both dyes enables the visualization of distinct spheroid layers, where Hoechst highlights the viable cells in the outer shell and PI selectively marks the necrotic core within. This dual-staining method effectively displays the structural organization within the spheroids. However, due to the toxicity of both fluorescent dyes, the stained spheroids cannot be reused for further experiments, rendering FLM a terminal analysis method.[32,35,36].

4.3 Transfection assays with spheroids

In addition to addressing various disease conditions, emerging gene therapy also enables a wide range of cancer treatment strategies. Gene therapy could be utilized to produce cancer vaccines, target specifically cancer cells, reduce the blood supply to the tumor or insert genes into cancer cells that revert them to normal phenotype. Transfection of cancer cells can be achieved by viral or non-viral vectors, the later can further divided into physical, chemical or biological methods. Regardless of the method employed, for a successful transfection the vector has to reach the crucial compartment within the cancer cell. Cellular uptake of vectors mainly occurs via endocytosis, where external substances are internalized into the cells. The effectiveness of transfection depends on the chosen targeted delivery system for the gene of interest[37].

4.3.1 Nanoparticle for spheroid transfection

One possible technique, that involves gene therapy, is utilizing nanoparticles (NPs) as targeted delivery system. NPs, containing the vector of interest, can be engineered using diverse structure assembling materials and molecules, such as lipids, polymers, dendrimers or gold elements. Their effectiveness in 3D cancer models is influenced by challenges like diffusion and penetration, necessitating careful optimization of NP properties. Key parameters encompass NP size, surface charge and surface functionalization. For example, smaller sized (<100 µm) NPs are able to penetrate deeper into the multicellular structure of 3D cancer models. Yet, for in-vivo treatment, particles under a specific diameter (<50 µm) show reduced circulation time and can lead to hepatocytes interaction as well as increased renal clearance. Additionally, the surface charge and incorporated functional groups impact the penetration and accumulation in 3D cancer cells models[38].

Chemical delivery systems such as nanoparticles, consisting of plasmid DNA or mRNA and polycationic polymers, are known as Polyplexes. An electrostatic interaction between positively charged polymers and negatively charged nucleic acids an electrostatic interaction takes place while mixing, resulting in the creation of core-shell type micelles. These Polyplexes demonstrate a high transferability, yet have a distinct cell toxic effect on cancer cells[39].

Among cationic polymers polyethyleneimine (PEI) is commonly used due to its numerous advantages. These including high cellular uptake, endosomal escape via the “proton sponge effect”, protection of nucleic acids from degradation, good water solubility and easy synthesis. PEI can be divided into two types: branched (BPEI) and linear (LPEI), with the later type having lesser toxic effect on the cancer cells. Damage to the cell membrane has a negative impact on the transfection efficiency. However, neither BPEI nor LPEI are biodegradable, contributing to the present cytotoxicity. To counterpart this, crosslinked LPEI (cLPEI) has been introduced as a more biocompatible alternative. Additionally, PEI can be further modified with PEGylation, enhancing stability and lessening the toxic effect on cells[40]

4.3.2 Transfection

For assessment of transfection efficacy, several methods are available. FLM allows direct visualization of transfected cells when fluorescent reporter genes, such as green fluorescent protein (GFP) and luciferase, are introduced. Furthermore, reporter genes can be straightforwardly analysed and monitored via readout devices. Flow cytometry enables the quantification of transfected cells utilizing fluorescently labelled antibodies. Another method involves Real Time PCR (qPCR), measuring the nucleic acids quantitatively in transfected cells. Alternatively, Western Blot method provides an indirect approach by analysing the expression of introduced proteins in cells[41].

The principle of luciferase assays is based on bioluminescence. Bioluminescence is a chemical reaction triggered by luciferases and their specific substrates that produces light. The light intensity than can easily be measured by photomultiplier or charge-coupled device camera. Cells introduced with different luciferase reporter genes, originating from the superfamiles *Cypridina* (CLuc), *Gaussia* (GLuc) and *Metridia* (MetLuc), express and secrete the enzyme. By addition of the respective substrate - luciferin for CLuc, coelenterazine for GLuc and MetLuc - the bioluminescence reaction is triggered, and the resulting light signal can be measured. Luciferase assays offer a highly quantitative and sensitive method with a minimal background for measuring the transfection efficiency [42].

4.3.3 Viability assays- resazurin assay

The assessment of viable and dead cells plays a crucial role in cell culture studies. Cell viability assays correlate the detected response to cell number, providing deeper insight into the health status and proliferation of cell cultures. These cell viability assays range widely and differ in their detection and act on the cells. The most prominent ones are metabolic dyes, such as MTT and resazurin, which are reduced by viable cells into measurable substrates. Alternatively, live/ dead staining offers another approach by distinguishing viable cells form dead ones via fluorescence or other detection methods. Additionally, cell viability also can be measured indirectly by lactate dehydrogenase (LDH) release into the supernatant, which indicates cell damage and death. The optimal

assay method depends on the cell type, culture conditions as well as desired experimental outcome to ensure accurate and relevant results [43].

Cell viability assays based on resazurin are highly sensitive and require short incubation time. Resazurin is a nontoxic blue dye that enters viable cells and is metabolically reduced to resorufin, a pink fluorescent substrate, which is secreted into the supernatant (Figure 8). The resulting fluorescent intensity can be easily measured (ex/em = 530-570/580-620 nm) and correlates directly to the number of viable cells. Resazurin cell viability assay has several advantages to MTT as it is more sensitive, less influenced by interfering compounds and nontoxic at low concentrations. Cells incubated with resazurin can be reused for further experiments, making this method versatile and reusable for prolonged settings [44].

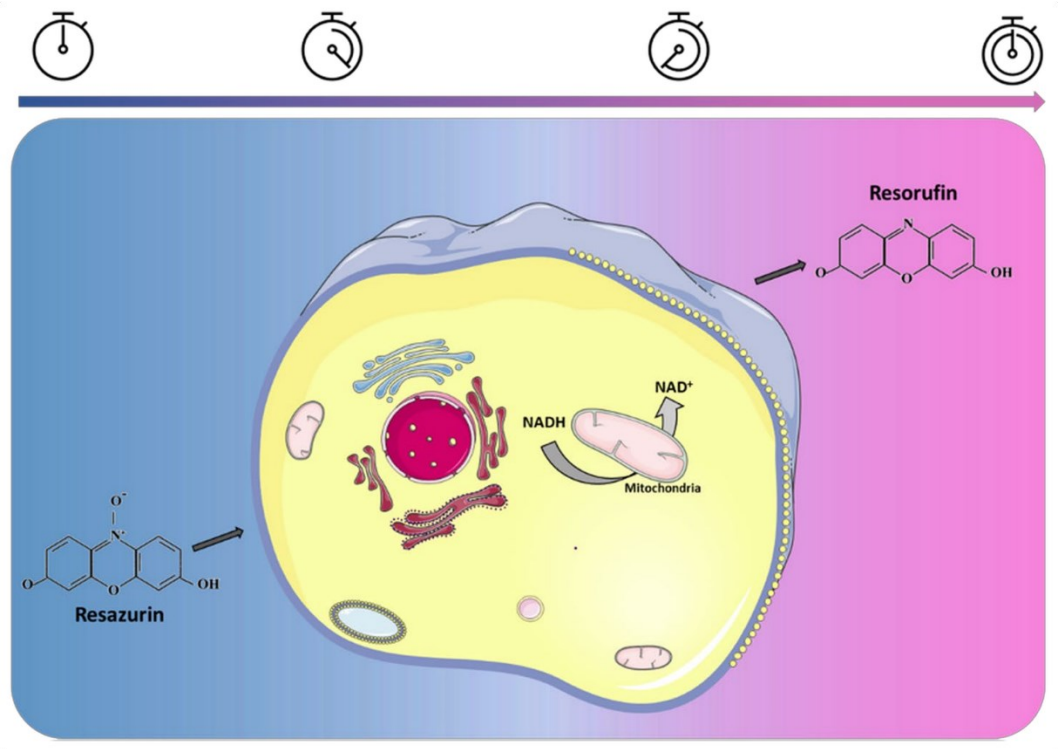

Figure 8: Resazurin reduction to resorufin in viable cells. Figure form Petiti et al[44].

5 Aim of Master Thesis

The present thesis focuses on three-dimensional (3D) cell spheroids for murine colon and breast cancer models. One of the main goals for the CT26Luc cell line (colon cancer) was to visualize the morphology and formation of necrotic core in 3D cancer cell spheroids. With increasing size, spheroids tend to establish an accumulation of dead cells, mostly in the centre of the spheroid. The focus was imaging the altering ratio of living and dead cells as well as the structural organization within the spheroids over the days. In addition to this, formate production as a metabolic byproduct was evaluated by measuring the concentration in the supernatant on designated timepoints. Furthermore, experiments were conducted to estimate the cytotoxic effect of Oxaliplatin on CT26Luc spheroids. The objective was to determine the extent of cell death induced by different concentrations of Oxaliplatin and the corresponding change in spheroid structure. Primary focus was to assess the shift in proportion of the necrotic core relative to the living cells. The second aim of this thesis was to study the transfectability of 3D cancer cell spheroids using GLuc transcribing pDNA and mRNA with various polymers. The Polyplexes were produced with either LPEI, pegylated LPEI or cLPEI at different N/P ratios. Main focus was to estimate the polyplexes that yield the highest transfection efficiency, producing the highest signal, while minimizing the cytotoxic effects on the spheroids which was measured by resazurin assay.

In the second project, 4T1-MTHFD1L cell line having a stable knockdown of methylenetetrahydrofolate dehydrogenase (MTHFD1L, a mitochondrial enzyme responsible for formate production) was compared with 4T1 SCR cell line (non-targeting control cells) by forming spheroids with a similar set of objectives. The primary aims were observation and visualization of the formation of the necrotic core spheroids of both cell lines. Similarly to the CT26Luc spheroids, the build-up of dead cells was predominantly found in the center of the spheroids over the prolonged experimental timeline. The main focus lied on the assessment of viable and dead cells and their structural distribution within the spheroids over the course of days. Additionally, the secreted formate in the supernatant was monitored by formate assay measurements on designated days. A further goal was to evaluate the transfection efficiency for 4T1 SCR spheroids, utilizing GLuc transcribing pDNA and mRNA in combination with various polymers. In a similar

pattern to the CT26Luc spheroids, Polyplexes consisting of LPEI, pegylated PLEI or cLPEI at different N/P ratios were tested. The objective was to determine the Polyplex formulations optimizing the highest transfectability with minimal cytotoxicity in the 3D spheroid model.

6 Materials

This section contains all the materials used with the corresponding manufacturer and specification.

6.1 Materials

All Materials used are shown in Table 1.

Table 1: List of materials used, including manufacturers.

Materials	Manufacturer
COSTAR ® 96-well Plate Ultra-Low Attachment (7007)	Corning Incorporated
CT15/50 tubes (LOT: 3043222/ LOT: 4041521)	Sarstedt
Cell culture T75 flask (LOT: 4021421)	Sarstedt
Sterile Syringe Filter 0,2 µm PES (LOT: 2312242201)	Fisher Scientific
SOFT-JECT® Luer single use syringe (10 mL) (LOT: 22B17C8)	VWR chemicals
small tubes (0.1, 0.5, 1.5, 2.0 mL)	Eppendorf
Pipette tips (10, 200, 300, 1000 µL)	Nerbe plus GmbH/ Eppendorf
Pipette boy	VWR International
Pipette (2.5, 10, 100, 200, 1000 µL)	Eppendorf and/or Sarstedt
Serological pipetts	Sarstedt
CELLSTAR 96-well, cell culture-treated, F-bottom microplate (white) (Ref: 655098)	Greiner BioOne
CELLSTAR 96-well, cell culture-treated, F-bottom microplate (clear) (Ref: 655180)	Greiner BioOne

6.2 Chemicals and kits

All chemicals and kits used are listed in Table 2 and Table 3.

Table 2: List of chemicals used, including manufacturers and usage.

Chemicals	Manufacturer	Usage
DMEM F-12 Ham (Cat# RNB4667)	Sigma Aldrich	Cell culture media
Gibco DMEM no glucose, no glutamine, no phenol red, no sodium pyruvate, (Cat# A1443001)	Sigma Aldrich	Cell culture media
Fetal calf serum, sterile filtered	MMCT	Cell culture media
Penicillin/Streptomycin (Cat# P0781)	Sigma Aldrich	Cell culture media
L-Glutamine (200 mM; Cat#: G7513)	Sigma Aldrich	Cell culture media
Gibco Tryp-LE express enzyme, phenol red (Cat# 12605028)	Thermo Fischer	Cell splitting
Dulbecco´s Phosphate Buffered Saline Modified (LOT: RNBM5276)	Sigma Aldrich	Cell culture
Glucose solution (200 mg/ml)	Sigma Aldrich	Cell culture media
Resazurin sodium salt (LOT: A041563)	Fisher Scientific	Resazurin assay
Collagen from calf skin (LOT: SLCD5043)	Sigma Aldrich	Spheroid formation (KP1 & KP2 experiment)
Methylcellulose, vicosity: 4,000cP (CAS-No: 9004-67-5)	Sigma Aldrich	Spheroid formation (KP Methly 1 & 2 experiment)

Hoechst 33342 (10 mg/ ml)	Sigma Aldrich	Necrotic core staining
Propidium iodide (1,0 mg/ ml) (CAS: 25535-16-4)	Sigma Aldrich	Necrotic core staining
MilliQ water	Sartorius	GloMax® cleaning
Ethanol (99%) absolute	Fisher scientific	GloMax® cleaning

Table 3: List of kits used, including specifications, manufacturers and usage.

Kit	Specification	Manufacturer	Usage
Formate Assay Kit (colometric)	LOT: WS0J002X7600, -20°C storage	NOVUS Biologicals	Formate assay

6.3 Cell lines

All cell lines employed are shown in Table 4.

Table 4: List of cell lines used, including manufacturers.

Type	Manufacturer
KP PGK eGFRLuc	MMCT
CT26Luc	MMCT
4T1 SCR	Luxembourg Institute of Health (LIH), Department of Cancer Research, Director of Department of Cancer Research Johannes Meiser
4T1-MTHFD1L	Luxembourg Institute of Health (LIH), Department of Cancer Research, Director of Department of Cancer Research Johannes Meiser

6.4 Media and buffer used for cell lines

All media and buffer used within this work are shown in Table 5, including specifications. All individual components are listed in Table 2.

Table 5:List of specifications of buffer and media used for cell lines.

Media/buffer	Specifications	Usage
Basal DMEM F-12 Ham	DMEM F-12 Ham	Transfections
cDMEM F-12 Ham	DMEM F-12 Ham, 10% FCS, 1% Penicillin/Streptomycin, 1% L-Glutamine	Cell culture
Basal DMEM (no glucose, no glutamine, no phenol red, no sodium pyruvate) for 4T1	DMEM no glucose, no glutamine, no phenol red, no sodium pyruvate	Transfections
cDMEM (no phenol red, no sodium pyruvate) for 4T1	DMEM no glucose, no glutamine, no phenol red, no sodium pyruvate, 10 % FCS, 1% Penicillin/Streptomycin, 1% L-Glutamine, 17 mM Glucose	Cell culture
HBG buffer	Sterile, pH 7,4, 5% Glucose, 20 mM HEPES	Transfections
NaCl 5 mM buffer	PBS, Natriumchlorid (Art.-Nr. P029.3, CAS: 7647-14-5, Manufacturer: Roth)	Gluc read out

6.5 Plasmids and Polymers

All plasmids and polymers employed within this work are listed in Table 6.

Table 6:List of plasmids and polymers used, including manufacturers.

Type	Manufacturer
cLPEI (cross linked = 0,5 factor, in vitro stock, 2 mg/mL in MQ, sterile filtered, DP1 batch SD 29.08.2022)	MMCT
LPEI 10k Da (2500 µg/mL in MQ, sterile filtered 0.2 µm, HS/ SD 12.08.2020)	MMCT
LPEIPeg2-Cys (130315AT, 937,7 µg/mL)	MMCT
GLuc mRNA 1 -BS (876,6 µg/mL, from IVT_EM_050224 experiment)	Produced by Ewelina Maslowska in MMCT
GLuc mRNA 3 -BS (1070,5 µg/mL, from IVT_EM_050224 experiment)	Produced by Ewelina Maslowska in MMCT
pCMV-GLuc pDNA (424,75 µg/mL, 28.11.23 ONC1 p2)	Produced by Ewelina Maslowska in MMCT

6.6 Devices

All devices used are listed in Table 7, including specifications and manufacturer.

Table 7: List of devices used, including specifications and manufacturers.

Devices	Specifications	Manufacturer
Waterbath	WNB29	MEMMERT
Counting chamber	0.1 mm depth, 0.0025 mm^2 (LOT: 08D, REF: 718005)	Marienfeld Brand GmBh
Microscope	IX73	Olympus
Sterile Hood	HerasafeTM KS (NSF) Class II, Type A2 Biological Safety Cabinet	Thermo Scientific™
Incubator	HeracellTM 150i CO2 Incubator	Thermo Scientific™
Vortex	Serial number: VB201AL0000198	Starlab

Scale	ABP 100-5DM	Kern
Centrifuge	Heraeus Megafuge 16R Centrifuge	Thermo Scientific™
Ep centrifuge	Mini fuge plus (Ref: N2631-0017)	Starlab
Plate reader	Infinite 200Pro	Tecan
Labelling machine	P-touch (2430PC)	Brother
Filter system fo MilliQ water	Arium® pro Ultrapure water system	Sartorius
Luminometer	GloMax Navigator with Dual I	Promega

6.7 Software

All software used are shown in Table 8.

Table 8: List of software used, including their purpose.

Software	**Purpose**
cellSens 2.2, Olympus	Phase contrast (PH)/ Fluorescence microscopy (FLM)
Glomax Navigator version 3.0	Gluc assay readout

7 Methods

This section provides an overview and description of all the methods used, emphasising the specific differences between both cell lines. Detailed overviews for each goal can be found in the appendix.

7.1 CT26Luc-based spheroids

7.1.1 Cell culture and spheroid seeding

Cell maintenance

The following steps were performed for cell maintenance: The cells were kept in a T75 cell culture flask and passaged regularly twice a week (Mo. and Fr.). Under normal circumstances the cells had a confluency of 80-95% prior to passaging/ cell splitting. For the passaging/ cell splitting, first the old media was removed, and the cells were washed with PBS (5 mL). Tryp-LE (1 mL) was added to detach the cells, and the flask was incubated in the incubator for 4 min (37°C). After incubation the flask was washed twice with fresh complete media (4 mL and 3 mL). On one hand, the media is needed to deactivate the trypsin, and, on the other hand, the cells are then brought into a liquid which can be transferred further. The cell suspension was passed on into a CT15 tube which then was centrifuged for 5 min (200xg, RT). Simultaneously, a new T75 flask was labelled and filled with fresh complete media (12 mL). After that the supernatant was discarded, and the cell pellet was resuspended in 1 mL fresh complete media. Based on the cell line a split ratio was estimated and according to this ratio a specific amount of µL of the cell suspension was then added to the new flask. To evenly distribute the cells in the new flask a ∞-motion was done, and the flask was put back again in the incubator until next split.

For the CT26Luc complete media containing F12-ham was used and split with a 1:20 ratio.

Cell counting

For the cell seeding nearly the same steps were done as for the cell splitting described at the section above. Instead of adding a specific volume to an additional new flask the cell

suspension was further diluted in fresh complete media (1:10-1:20,). 2x 10 µL of this diluted cell suspension were then transferred onto a counting chamber. To achieve precise counting, it is essential to ensure that each square contains at least 30 cells. The grid engraved into the counting chamber was used for orientation while counting. The counting went as imaged in Figure 9: only the cells in the white chambers were considered. Cells that were sitting on the bold lines were included while the cells on the thin lines were excluded for counting.

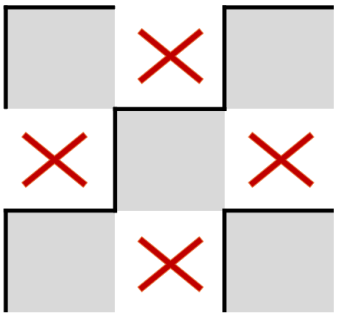

Figure 9: Grid for counting. Only the highlighted fields in grey were counted including the bold lines.

Afterwards, the sum of all counted chambers was calculated and averaged (divided by 10). The average was then used in the following equation to determine the approximate number of cells in the original suspension (1 mL):

$$c_{cells}\ orig = \emptyset * DF * 10\ 000$$

$c_{cells}\ orig$ … Cell concentration in original suspension [cells/mL]

$\emptyset$ … Average cell count in the counting chamber

DF … Dilution factor

Spheroid seeding

Based on the cell concentration in the original suspension the needed cell amount for seeding can be calculated with this formular:

$$Suspension\ volume\ needed\ per\ well = \frac{desired\ cell\ count/well}{cell\ count/mL\ of\ prepared\ dilution} \times 1000$$

Subsequently, the needed suspension volume was added to the wells. Depending on the volume used, the remaining volume was adjusted to 200 µL with complete media. This procedure was applied for both 2D, and 3D cell seeding. The difference was the plate where the cells were seeded in (shown in Figure 10). For 2D cell culture standard flat (F) plates were used, however, to prevent the natural phenomenon of the cells adhering to the surface, another plate must be used. The ultralow attachment plates are designed so that the cells are physically not able to align on the surface. This way they are forced to adhere to each other. The day on which spheroids are seeded is designated as day 0.

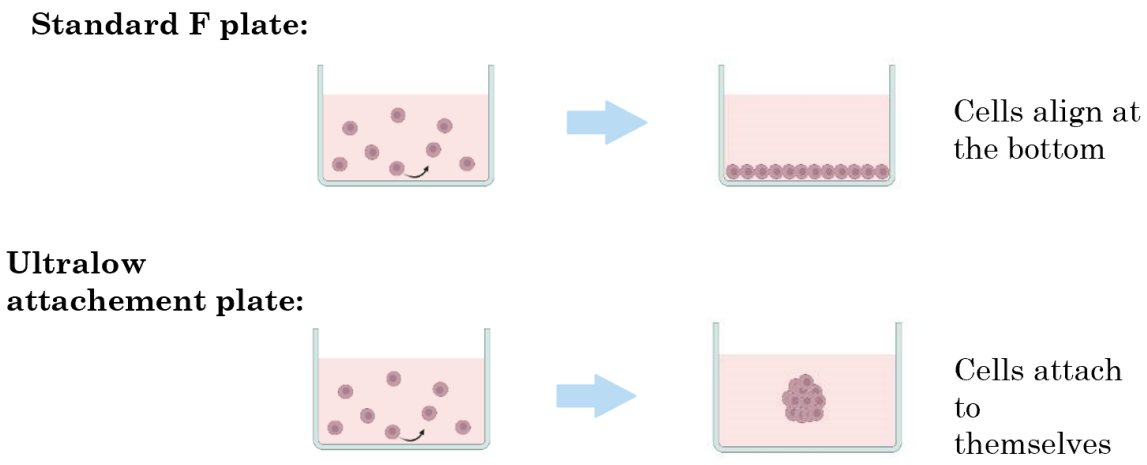

Figure 10: Spheroid formation in low-attachment plates: Normally the cells would align at the bottom of the well. However, the low-attachment plates hinder the cells to attach to the surface. This way they are forced to adhere to themselves (created with Biorender).

7.1.2 Phase contrast microscopy

The spheroids in the wells were checked in the microscope after seeding. A magnification of 10x was used for checking and capturing images. These images were further processed using the cellSens 2.0 software. Phase contrast images were taken either alternate days or prior to planed experiments to monitor spheroid growth.

7.1.3 Resazurin assay

For the cell viability assay, the resazurin solution first must be prepared. As Resazurin is highly light-sensitive, all the steps of the workflow must be carried out under minimal light exposure. All tubes and Eppendorfer tubes used were covered in aluminium foil to protect it from the light. The procedure began by weighing in a minimum of 5 mg of resazurin powder in an epi (1.5 mL or 2.0 mL). After that the same amount of PBS in mL was used to dissolve the resazurin powder. The dissolved resazurin was transferred step by step to a CT15 tube. To ensure that the resazurin has fully dissolved the tube must be vortexed for about ten seconds. Next, an additional CT15 tube with 4 500 µL PBS was prepared beforehand and 500 µL of the vortexed resazurin solution was added to this. To make sure that the solution is mixed homogenously it must be vortexed again for few seconds. In the meantime, a third CT15 tube, a 10 mL sterile syringe and a 0,2 µm PES sterile filter were prepared in the hood. The syringe was placed on the filter and held over the additional CT15 tube while the freshly mixed resazurin solution was poured in and filtered into the tube. The concentration of the freshly prepared resazurin solution was 0,1 mg/mL. Until usage the tube must be protected from light.

In the selected wells, the 200 µL old media was removed first and 108 µL of fresh complete media were added. Following that, 12 µL of resazurin solution were added (concentration of 10% resazurin/ well) and the plate was put back again in the incubator for 4h. To differentiate the background signal from the cell viability a control group of three blank wells was consistently treated and measured under the same conditions. After the incubation period 100 µL of supernatant were transferred to a clear 96 standard F well plate which was then again covered in tinfoil until readout. If the spheroids are being used again remaining resazurin supernatant in the wells was removed and 200 µL fresh complete media was added in.

Readout was done with the Tecan plate reader as follows with parameters shown in Table 9:

Table 9: Measurement parameters for fluorescence readout.

Parameter	**Setting**
Measurement Mode	Fluorescence measurement from below

Excitation Wavelength	560 nm
Emission Wavelength	590 nm
Excitation Bandwidth	9 nm
Emission Bandwidth	20 nm
Gain	90 (Optimal, 100%)
Number of Flashes	25
Integration Time	20 µs
Delay Time	0 µs
Rest Time	0 ms

The Resazurin based cell viability assay were typically performed alternate days in the selected experiments. However, depending on the specific requirements and goals of each experiment the frequency was adjusted as needed.

7.1.4 Necrotic core staining and fluorescent microscopy

For the necrotic core staining two different substances were used.

Firstly, Hoechst which stains the metabolically active cells and is visible in the FLM as blue colour (emission wavelength = 461 nm) after stimulation with fluorescent light. The staining solution was prepared in fresh media with a concentration of 160µg/mL to reach a final concentration of 8 µg/mL in the well. The calculation of the required amount of staining solution was carried out using this formula:

$$160\mu\frac{g}{mL}(stock\ conecentration) * x\ (needed\ \mu L\ of\ dilution)$$
$$= 10000\mu g/mL * y\ (\mu L\ of\ stock)$$

The actual necrotic core of the spheroids was stained with PI. It is not permeant to live cells and affects only the dead ones. In the FLM it appears as yellow colour (emission wavelength = 617 nm) after stimulation. The PI stock solution had a concentration of 1

mg/mL and was directly used without further dilution. The final concentration of PI in the well amounted to 50 µg/mL.

The staining workflow outlined as follows: In the designated wells the old media was changed with 180 µL fresh complete media. 10 µL of the prepared Hoechst solution and 10 µL of the PI stock solution were added to the wells resulting in a total of 200 µL. The plate was then put back in the incubator for 2 h. After the incubation time the read out was done at the FLM. For Hoechst the DAPI filter was used with an exposure time of 80 ms. When doing Z-stacks (images of the layers of the spheroids are captured at intervals of 10 µm) the exposure time was reduced to 10 ms. PI is detected with the Cy3 filter with an exposure time of 10 ms and for Z-stacks reduced to 5 ms. Captured images were again processed with the cellSens 2.0 software.

Necrotic core staining and visualization were done typically on alternate days in the selected experiments. Depending on the specific aim and objectives of the experiment the frequency was adjusted.

7.1.5 Formate assay

The formate assay was done with the kit from Novus® Biologicals. The read out of the collected supernatant was carried out according to the instructions in the operating manual. A standard curve was conducted for each experiment to ensure accurate formate quantification.

7.1.6 Effect of Oxaliplatin on cell spheroids

This experiment layout was outlined to investigate the cytotoxic effects of oxaliplatin on cancer cell spheroids. Various concentrations of Oxaliplatin, dissolved in PBS were added to the spheroids and treatments were carried out for either 24h or 48h. Spheroids at days 5, 6 and 7 of growth were used.

For the preparation of the Oxaliplatin treatment, a stock solution with a concentration of 4 mM Oxaliplatin in PBS was first prepared. From this stock, four sequential dilutions were made as follows:

1. First dilution with a concentration of 400µM: 300 µL of the stock solution was diluted with 2 700 µL of PBS
2. Second dilution (conc. 200 µM): 1 500 µL of the first dilution was mixed with an equal volume of 1 500 µL of PBS.
3. Third dilution (conc. 100 µM): 1 500 µL of the second dilution was mixed with an equal volume of PBS
4. Fourth dilution (conc. 50 µL): 1 500 µL of the third dilution was mixed with an equal volume of PBS.

Prior to starting the dilutions, the stock solution was vortexed to ensure a homogenous mixture. After each dilution step, the volumes were thoroughly re-suspended using the pipet.

In the meantime, the designated wells were emptied of the existing media and 100 µL fresh complete media were added. To these wells, 100 µL of the desired concentration of the oxaliplatin was added. Five wells were treated either 24 h or 48 h with the respective concentration of each dilution. Control groups, consisting of five wells either with only fresh media or a 1:1 mixture of fresh media and PBS, were kept for comparison. The control group with the 1:1 mixture of fresh media and PBS was done to ensure what toxic effect PBS might have on the cells.

Read out was done with GloMax® with the following parameters (Table 10):

Table 10:Measurement parameters for Glomax® readout.

Injection	
Injector	1
Volume (uL)	50
Speed (uL/s)	200
Wait	
Duration	00:00:02
Luminescence	
Emission Filter	None
Integration Time(s):	10
Reading	1

7.1.7 Transfection of spheroids

Polyplexing

For the transfection first the desired Polyplexes had to be produced as shown in Figure 11. Polyplexes consist of a specified mixture of nucleic acids (either pDNA or mRNA) and polymers. As aqueous solution HBG buffer was used. Required pDNA and/or mRNA were taken out of the fridge or freezer, flipped, spined down and added to a prepared volume of HBG buffer to prepare the mother stock. Likewise, the frozen polymer was taken out of the freezer, thawed, flipped, spined down and the precalculated amount was added to HBG buffer to obtain the mother stock. The prepared mother stocks then were flipped, spined down again and further diluted with HBG buffer (C1/P1). The mRNA and pDNA mother stocks should be stored at 4°C until the polyplexing process to prevent them from degrading prematurely. For producing the final Polyplexes the polymer dilution was added and mixed with the diluted nucleic acid ten times at normal speed and afterwards fifteen times with flash pipetting. After producing the final Polyplexes, they had to be added to the wells as fast as possible (< 30 min) to reduce risk of premature degradation.

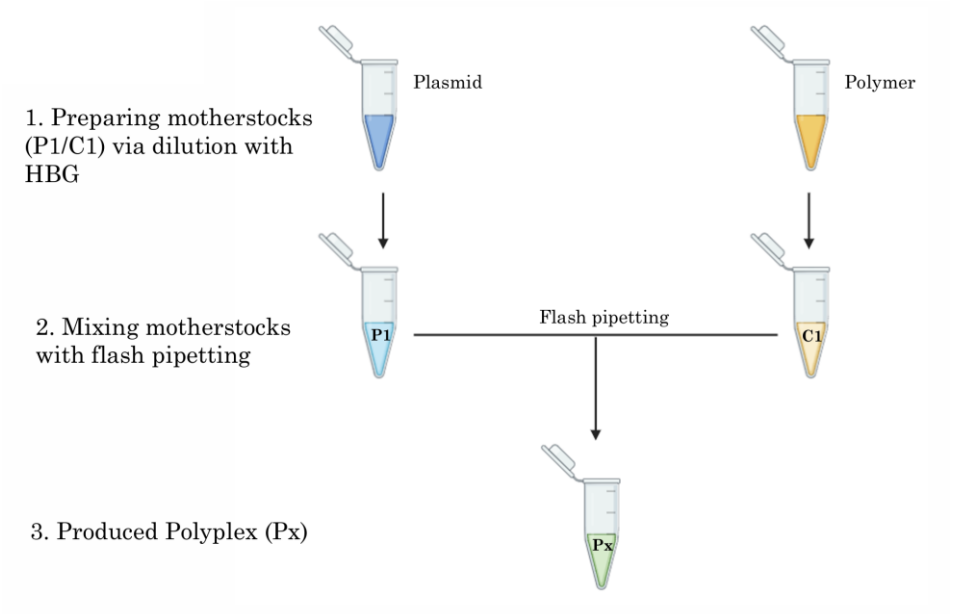

Figure 11: Preparation of Polyplexes. Firstly, the plasmid and polymer mother stocks were prepared via dilution with HBG buffer. To produce the finale Polyplexes, both previously prepared mother stocks were mixed together (created by Biorender).

Meanwhile, the old media from designated wells was removed and 75 µL of fresh basal media was added. Basal media is essential while adding the Polyplexes to the spheroids. This is to ensure that the Polyplexes do not form complexes with hormones, growth factors or other macromolecules which are present in complete media and thus result in reduced transfection rate. 25 µL of the solution containing the final Polyplexes was then added to the wells, resulting in a total volume of 100 µL. For the control group, 25 µL HBG buffer was added. The plate was then put in the incubator for 2 h. Afterwards, 100 µL of fresh complete media was added to the treated wells, resulting in a total volume of 200 µL per well. The plate then was put back again into the incubator for the desired incubation time, typically 24 h until the readout.

For the multiple CT26Luc transfection experiments the following Polyplexes were produced and used for transfection (Table 11):

Table 11: Employed nucleic acids and polymers including N/P ratio for producing Polyplexes for CT26Luc transfections.

Nucleic acid used	Polymer used	N/P ratio
GLuc-mRNA	cLPEI 0,5	12
	LPEI10kDa-PEG-Cys	
GLuc-pDNA	cLPEI 0,5	9
	cLPEI 0,5	12
	LPEI10kDa-PEG-Cys	

GLuc assay

To determine the intensity of signal and efficiency of the transfection, the GloMax® was used for readout.

Prior to the readout, the injectors of the GloMax® must be cleaned with MilliQ water, with Ethanol 70%, MilliQ water and lastly with air, as intended for the device.

Additionally, coelenterazine was needed as a substrate for GLuc to produce a luminescent signal which then can be measured. To prepare the required coelenterazine solution the aliquoted homemade coelenterazine (conc. 5 mg/mL) was taken out of the -80°C freezer. The whole preparation procedure must be under a minimal light source as coelenterazine is highly light-sensitive. Firstly, 4 991,53 µL NaCl (5 mM) solution was

prepared in a CT15 tube and 8,47 µL of the thawn coelenterazine was added. To mix it well the tube was vortexed for few seconds. The tube was then left aside to autooxidate (min. 30 min, max, 2 h, RT). The prepared solution must be shielded from the light until usage. After the autoxidation process the injector 1 of the GloMax® was primed with it and the device was ready for the readout.

For the GLuc assay only a small amount of supernatant of the incubated spheroids was required. Specifically, 20 µL of the supernatant were transferred to a white 96 standard F plate, which then was put into the GloMax® for readout.

7.2 4T1 SCR & MTHFD1L-based spheroids

7.2.1 Cell culture and spheroid seeding

The methods used for cell culture and spheroid seeding are identical to those described in section 7.1.1. Specific differences to this cell line are as follows:

1. Confluency and splitting: Prior to splitting, the confluency of 4T1 SCR & MTHFD1L amounted to 70-95%. An initial splitting ratio of 1:10 was used, followed by 1:20. For this cell line complete media without phenol red was used.
2. Cell counting and spheroid seeding: In contrast to CT26Luc cells, the 4T1 cell lines exhibited stronger adhesion and aggregation, which made precise seeding more challenging.

7.2.2 Phase contrast microscopy

Refer to section 7.1.2.

7.2.3 Resazurin assay

The preparation of the resazurin solution and execution of the cell viability assay were done identically as referred in section 7.2.3. The only difference between the cell lines was the use of different complete media.

In addition to this, the frequency of the conduction of the assay were kept the same. However, minor adjustments were made related to the specific experimental design.

7.2.4 Necrotic core fluorescence microscopy

The necrotic core work process was identical as described in section 7.2.4. Again, only the used complete media was different due to cell specific reasons. Therefore, Hoechst was diluted with fresh complete media without phenol red.

Necrotic core staining and visualization were done typically on alternate days in the selected experiments. Depending on the specific aim and objectives of the experiment, the frequency was adjusted.

7.2.5 Formate assay

The desired supernatant of the spheroids was collected and pooled consistently from ten wells. The formate concentration in the supernatant of the 4T1 spheroids was measured parallel to the supernatant of the CT26Luc spheroids.

7.2.6 Transfection of spheroids

The transfection process and production of the Polyplexes was done exactly as referred in section 0.

Again, the difference layed in the complete media used.

The following polyplexes (Table 12) were used for the experiments:

Table 12: Employed nucleic acids and polymers including N/P ratio for producing Polyplexes for 4T1 SCR transfections.

Nucleic acid used	Polymer used	N/P ratio
GLuc-mRNA	cLPEI 0,5 N/P 9	9
	cLPEI 0,5 N/P 12	12
	LPEI10kDa-PEG-Cys	
GLuc-pDNA	cLPEI 0,5 N/P 9	9

	cLPEI 0,5 N/P 12	12
	LPEI10kDa-PEG-Cys	

8 Results and Discussion

The results of the experiments of this master thesis are separated by their aims and cell line.

8.1 CT26Luc colon cancer spheroids

8.1.1 Necrotic core visualization and formate production

This section contains the experiments conducted to address this aim.

Optimization of spheroid characterization

The aim of this experiment was to form compact spheroids with the CT26Luc cell line and to estimate the cell viability with resazurin assay on alternate days. For this purpose, 5K based and 10K based cells were seeded. Phase contrast images of the wells were captured prior to conducting the resazurin assay. Furthermore, supernatant from day 39 of this experiment was collected for formate assay, and spheroids were harvested at the end of the experiment for Tissue Tek®.

As shown in the phase contrast images in Figure 12, the spheroids formed successfully. Over the course of the experiment, the spheroids increased in size significantly. The formed spheroids were rather spherical and looked compact. No lightly attached cells were observed. In few cases, fibres in the wells were observed, which adhered the cells and got incorporated into the spheroid. At some point in the whole experiment of the spheroid growth, the size of the 5K and 10K spheroids aligned, with an outlier in well B4.

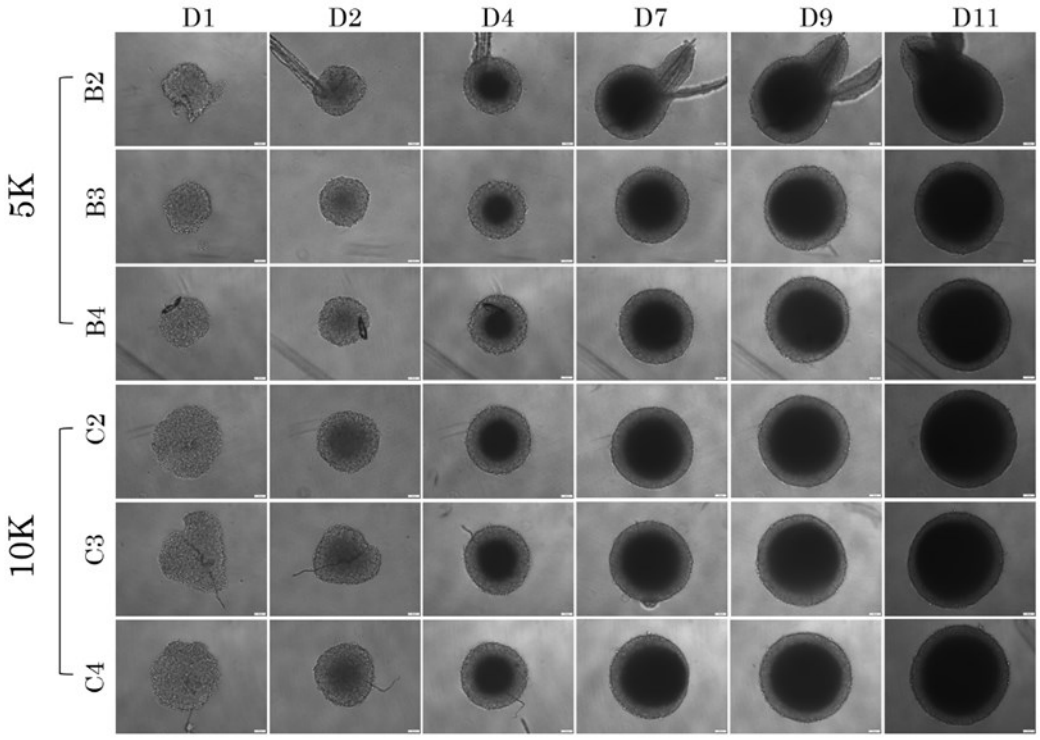

Figure 12: Phase contrast microscopy images of CT26Luc spheroids from two cell numbers (5K and 10K) at different durations of growth, as per the indicated timepoints. Three replicates (labelled with their well numbers) are shown from n=5 spheroids. D=day; images with automatic exposure, 10x magnification, scale bar size: 100 µm.

Although the spheroids looked similar in form and size, the presence of fibres in the well changed the morphological appearance of some spheroids. Additionally, even though the same conditions were kept for all spheroids, there was still a deviation in growth when comparing. Especially seen in well B4 (Figure A 1 and Figure A 2), at day 18 and onwards the spheroid increased in size more rapidly than the other 5K based spheroids, even surpassing the 10K based spheroids. As shown, various factors influence the uniformity of the cancer cell spheroids. Beside the cell density employed, individual interactions between single cancer cells as well as their environment in the well can cause variability in formation and growth, ultimately posing challenges to reproducibility[29]. For further experiments, the optimized imaging workflow was used and only 5K based spheroids were employed.

The viability of cells was estimated within the spheroids by resazurin assay. Due to technical issues with the plate reader in the beginning of the experiment, only data collected from day 11 onward were deemed comparable.

The cell viability is shown in Figure A 3. The data of the resazurin assay was very inconsistent. As the data shows the 5K and 10K spheroids gave similar signals for cell viability. The initial signal on day 11 was relatively high compared to the rest of the observed days. On day 15 a drop in cell viability could be seen. Between day 18 and day 30 the signal remained relatively stable, with a slight decrease noted over time. However, the last three datapoints displayed extreme outliers, which could not be explained within the experimental framework. Additionally, the standard deviation increased with the growth of the spheroids.

The outliers might be reasoned due to external factors. Since resazurin is a very light sensitive substance, unintentional overexposure to light sources could have been one possible cause. Additionally, as the standard deviation was increasing over the time and the spheroids had an individual growth pace, precise comparison was not possible. Another factor could be the incorporation of fibres. The cells favourably grew on present surfaces with fibres increasing the possible space to extend.

Necrotic core staining and formate production

The goal was to form compact spheroids to visualize the necrotic core formation and correlate it with phase contrast microscopy and viability. A total of 60 wells were seeded with 5K cells/spheroids. The workflow of the staining and FLM readout are described in section 7.1.4. Necrotic core staining was conducted on the days: 2, 4, 7, 9, 11, 14, 16, 18 and 21. Cell viability of the spheroids was performed with resazurin assay on alternate days and phase contrast images were captured prior. Additionally, the supernatant of 10 wells was collected and pooled for formate assay the following days: 2, 4, 7, 9, 11, 14, 16, 18 and 21. Also, transfections were performed on day 16 and 22. Transfection results will be presented and discussed in section 8.1.3. Further details can be found in the appendix.

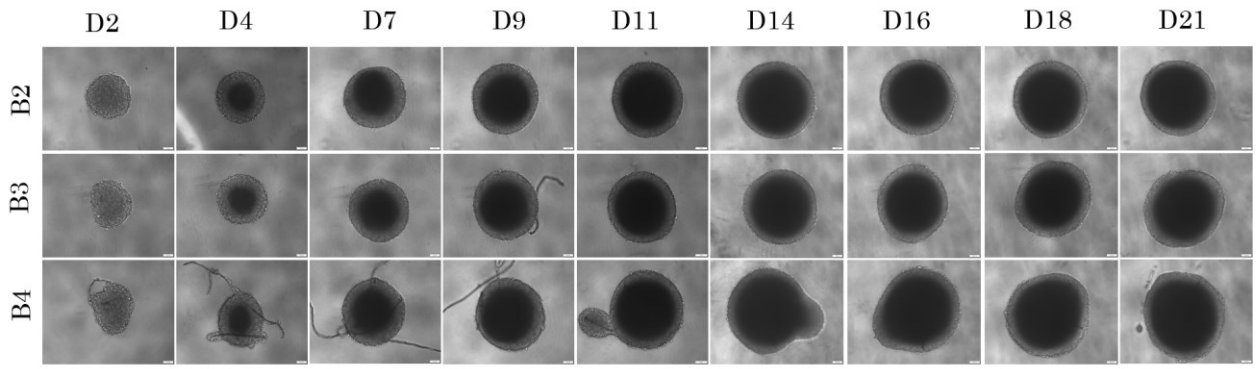

Figure 13 :Phase contrast microscopy images of 5K CT26Luc spheroids at different durations of growth, as per the indicated timepoints. Experiment was done with three replicates (labelled with their well numbers). D=day; images with automatic exposure. 10x magnification, scale bar size: 100 µm.

As the images show (Figure 13), the spheroids formed successfully and exhibited continuous growth over time. In addition to this, Figure 14 shows that the signal in cell viability increased and reached its peak on day 11. Until day 16, a decrease can be observed, followed by an increase until D21.

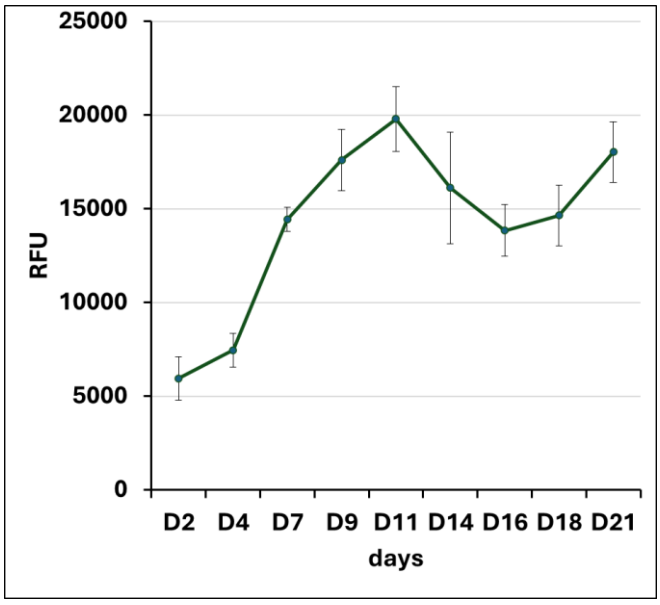

Figure 14: Relative fluorescence signal as RFU through resazurin cell viability assay of CT26Luc spheroids with an initial seeding number of 5K cells. The shown RFU is average of N=3 spheroids with one measurement per spheroid.

For the staining results, different foci of the images were captured, which can be seen in Figure 15. While the chosen perspective does affect the results, the necrotic core shown in yellow is more clearly visible from the middle most section. Therefore, all subsequent images in this thesis will be presented form this perspective to enhance clarity.

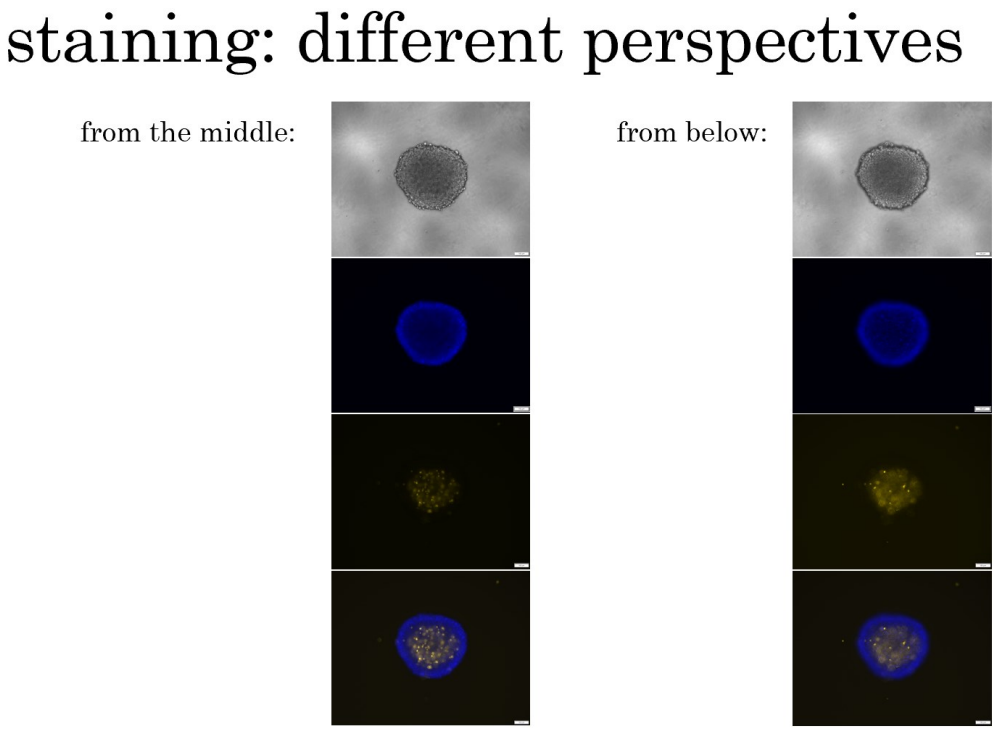

Figure 15: Different perspectives for live/ dead staining with Hoechst and propidium iodide (PI) via fluorescence microscopy (FLM). The left column demonstrates the images of the stained spheroid form the assumed middle perspective. The right column displays the same spheroid from the perspective below. Shown are phase contrast microscopy images (exposure time=10 ms), Hoechst staining (conc.8 µg/mL, exposure time=80 ms) with DAPI filter, PI staining (conc. 50 µg/mL, exposure time=10 ms) with Cy3 filter, and an overlay of Hoechst and PI, in descending order. 2 h incubation time for staining solutions.

As shown in Figure 16, the necrotic core already started to form on day 2. The necrotic core grew in proportion to the increasing size of the spheroids leaving only a distinct layer of viable cells, highlighted in blue, in the outer shell.

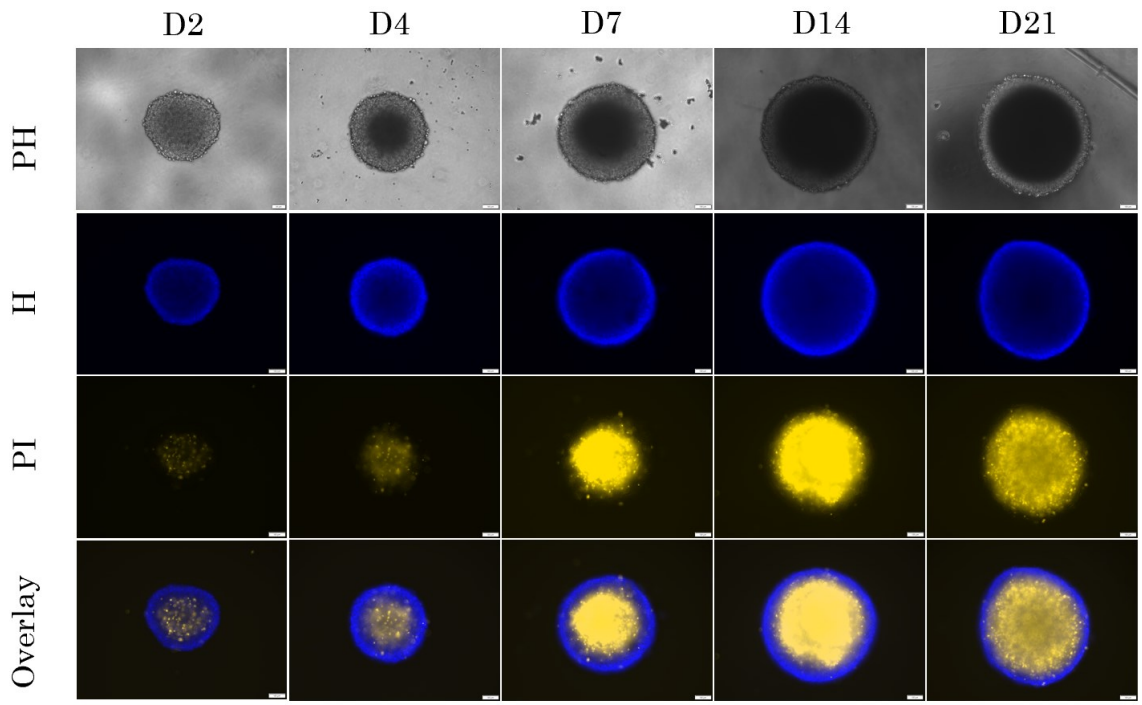

Figure 16: Necrotic core staining of CT26Luc spheroids imaged via fluorescence microscopy (FLM) in descending order: PH (phase contrast, automatic exposure time), H for Hoechst (conc. 8 µg/mL, exposure time=80 ms) with DAPI filter, PI for propidium iodide (50 µg/mL, exposure time=10 ms) with Cy3 filter, and an overlay of both staining methods. 2 h incubation time for staining solutions; D=day; The shown images are representative images from N=2 spheroids.

Due to this, it is clearer to see why the measured cell viability stagnates at some point of growth. With increasing size, the formation and extension of the necrotic core become evident. Based on the FLM images, the relatively low increase in cell viability can be attributed to the expansion of the necrotic core, which as a result limits the overall number of viable cells. The observation in drop of fluorescence signal in the resazurin assay on day 16 might not be due to external factors but rather a natural process driven by the spheroid ´s growth dynamics. Another important factor to consider is that the outer cell layer of the spheroids has a higher metabolic activity compared to the hypoxic quiescent cells located between the outer layer and the already necrotic core. Bigger spheroids consist of a significantly higher population of quiescent cancer cells, which may not be accurately detected by metabolically active substances[45].

Formate concentration in the pooled supernatant was evaluated at the designated time points indicated in Figure 17 using the formate assay kit. The final formate concentrations were interpolated form the concurrently generated standard curve, as the read-out of the

formate assay kit is absorbance-based. The graph (Figure 17) shows an evident increase in formate concentration over the measured days. On day 16 the formate concentration was nearly fivefold higher compared to day 4.

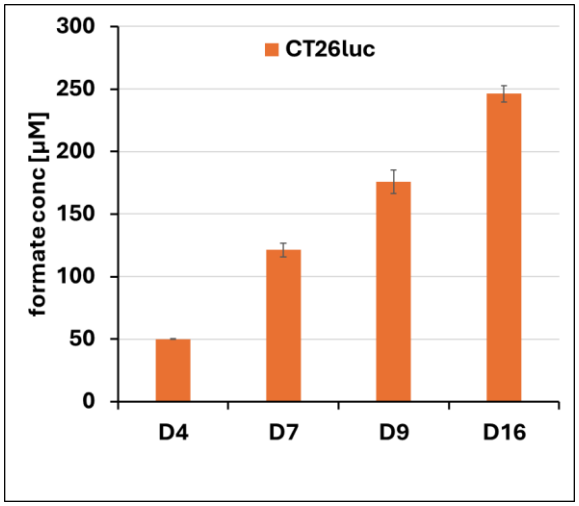

Figure 17: Formate assay evaluation of CT26Luc spheroids. The pooled supernatant of the spheroids was measured on days 4, 7, 9, and 16. Supernatant pooled form 10 spheroids was measured in triplicates.

As the data demonstrates the formate detection worked. However, as no additional metabolic studies were conducted, it cannot be conclusively determined, whether a specific pathway is upregulated and leading to excessive formate overflow.

8.1.2 Effect of Oxaliplatin on spheroid growth and necrotic core

The data presented for this aim is a representative experiment from three such experiments.

The aim of this experiment was to identify the effects of various concentrations of oxaliplatin on spheroids. Two plates of spheroids with a cell amount of 5K were seeded. To distinguish the exact effects four different concentrations of oxaliplatin (25, 50, 100, 200 µM) were tested on different days and for different incubation times (24 h, 48 h). As a control group completely untreated and PBS treated spheroids were kept simultaneously. Phase contrast microscopy images were captured prior and after the intended incubation

time to monitor the effects of oxaliplatin. Cell viability and necrotic core staining were estimated after the intended incubation time.

The spheroids prior treatments are shown in the top row of Figure 18, representing the days 5, 6, and 7 of growth. Below each pre-treatment image, first the PBS treated control group and the spheroids with different concentrations of oxaliplatin are displayed, both 24 h and 48 h post-treatment. For each timepoint, representative images of the corresponding control group and increasing concentrations are shown.

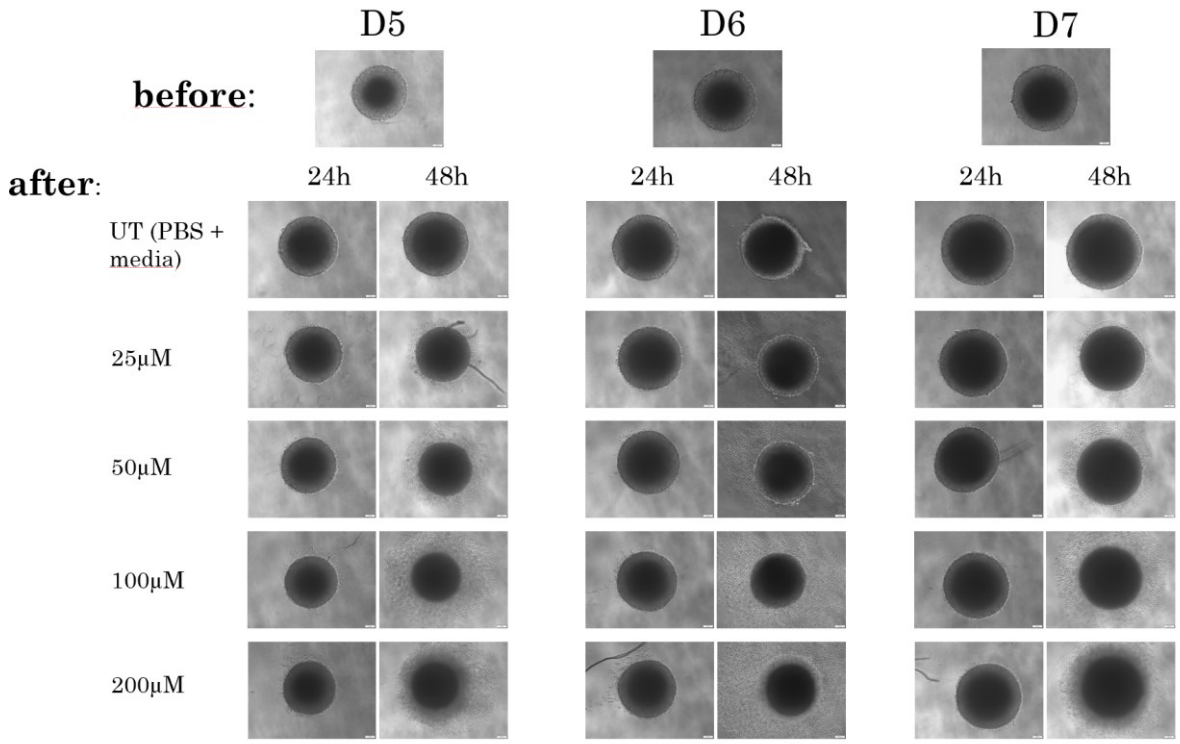

Figure 18: Phase contrast microscopy images of Oxaliplatin treatment in CT26Luc spheroids. The top row shows phase contrast images of the spheroids prior to treatment on the designated days. The treatment consisted of a treatment duration of 24 h or 48 h with various concentrations of Oxaliplatin added to the wells. Control groups, treated with a mixture of 1:1 PBS and media respectively are also shown. Images were taken from one out of three experiment. N=9; automatic exposure time; D=day.

As the images suggest, longer incubation times and higher concentrations of oxaliplatin lead to cell death. This is visible by the difference in cell morphology of the outer shell. The spheroids lose their compact form, and apoptotic cells can be seen floating scattered

around. In contrast to that, the PBS treated control group resembles the pre-treatment spheroids, showing no visible difference in morphology.

Figure 19 is structured according to the same scheme as Figure 18. Besides the necrotic core staining, PI was used here to highlight the dead cells effected by the oxaliplatin. With increased concentration and incubation time the yellow fluorescent PI is more evident, leading to individual staining points appearing in the viable outer shell of the spheroids. At some point it overshadows the blue fluorescent Hoechst, progressively increasing in number and intensity, until the spheroids appear completely yellow. This indicates the toxic potential of oxaliplatin.

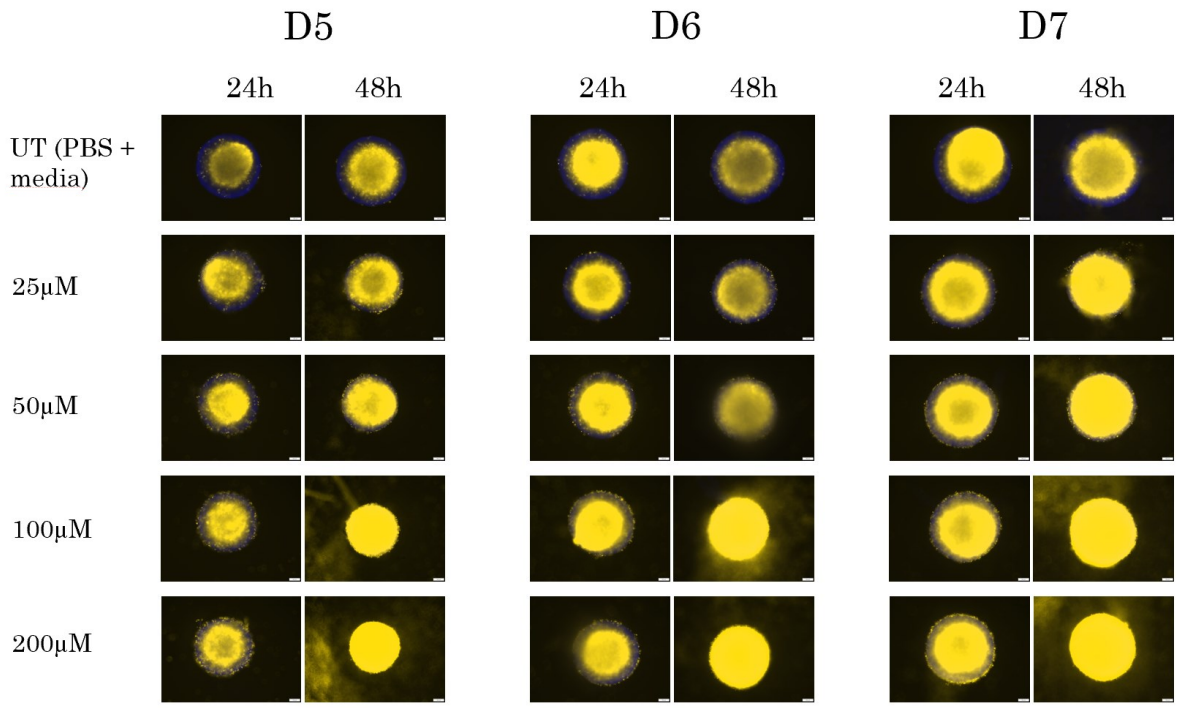

Figure 19: Live/dead staining after Oxaliplatin treatment of CT26Luc spheroids via fluorescence microscopy (FLM). The spheroids were stained with Hoechst (H, conc. 8 µg/mL) and propidium iodide (PI, conc. 50 µg/mL) after 24 or h 48 h treatment with various Oxaliplatin concentrations. Images were extracted from the Z-stacks done of the 3 experiments (exposure time 10 ms with DAPI filter and 5 ms with Cy3 filter for H and PI respectively). 2 h incubation time for staining solutions; N=6. The shown images are representative images from three experiments with tow spheroids per experiment.

Figure 20 shows the compilation of the cell viability of all three experimental layouts. Per day section, the control group as well as the different concentrations are displayed in

alignment. Two different bars corresponding to the respective incubation time are presented. The data was standardized to the control group of completely untreated spheroids, which were not shown in this abstract. An overall decrease in cell viability with increasing concentration of oxaliplatin is evident in the graph, with lesser signal measured for spheroids treated for 48 h. Additionally, the PBS-treated control group for 48 h exhibited a slightly reduced signal on days 5 and 6, indicating that the 1:1 mixture of media and PBS has a minor impact on the cell viability of the spheroids. Spheroids on day 7, treated either 24 h or 48 h, seemed indifferent to that. The spheroids on day 6 in general were the least effected by oxaliplatin (24 and 48 h treatment) when compared to the other days.

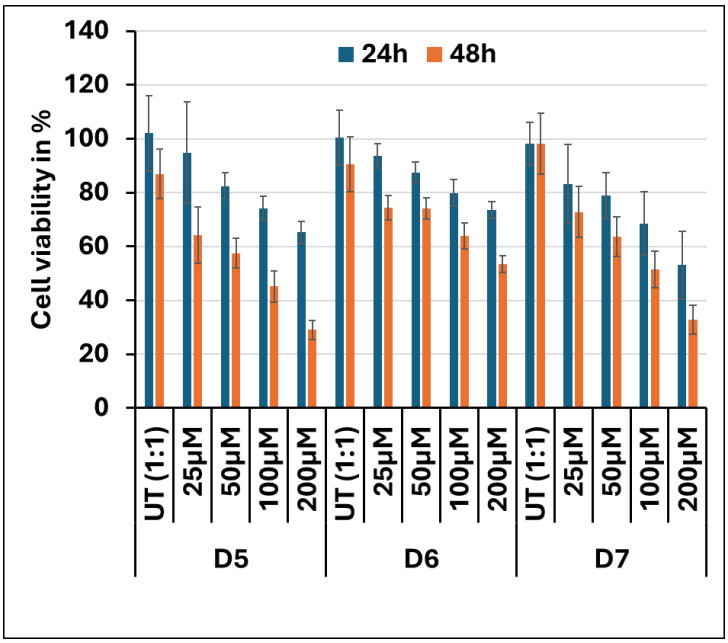

Figure 20: Relative fluorescence signal as RFU through resazurin cell viability assay of Oxaliplatin treated CT26Luc spheroids compared to untreated cells. The graph encompasses the viability signal of all three experiments averaged and normalized to untreated spheroids. N=9 spheroids one measurement per spheroid.

These results suggest that oxaliplatin has a dose and time dependent effect on spheroids. With lesser concentration and incubation, the toxic effect is less evident when compared to higher concentration and longer incubation time. Progressive disintegration of the spheroid structure can be observed with phase contrast images and the staining readout. Interestingly, the spheroids treated on day 6 were least affected by the oxaliplatin. This

might suggest that particular growth phases of cancer may react with different sensitivities to administered cancer therapeutics.

8.1.3 Transfectability of spheroids

Optimization

The experimental layout was previously outlined in *Necrotic core staining and formate production* in section 8.1.1. The goal of this experiment was to identify the transfection rate achieved with different Polyplex formulations and to optimize the workflow. A key objective was to assess, whether extended incubation (exceeding 24 h) with Polyplexes leads to higher transfection efficiency.

On day 22 of spheroid growth, spheroids were transfected with GLuc-pDNA LPEI N/P 12 Polyplexes, varying only in the amount of GLuc-pDNA added per well. For the first experiment, LPEI 10kDa was used as it has good transfection performance in 2D cell culture. Two different supernatant harvesting time points, 24 h and 72 h post-transfections, were analysed. As the data displays, the intensity of the signals for the lowest amount were for both harvesting times points quite similar. However, comparing the other datapoints, the transfection rate was less pronounced at the 72 h harvesting time. In general, the wells that received 1000 ng/well of pDNA and had their supernatant collected at 24 h exhibited the highest transfection rate. The results are shown in Figure 21.

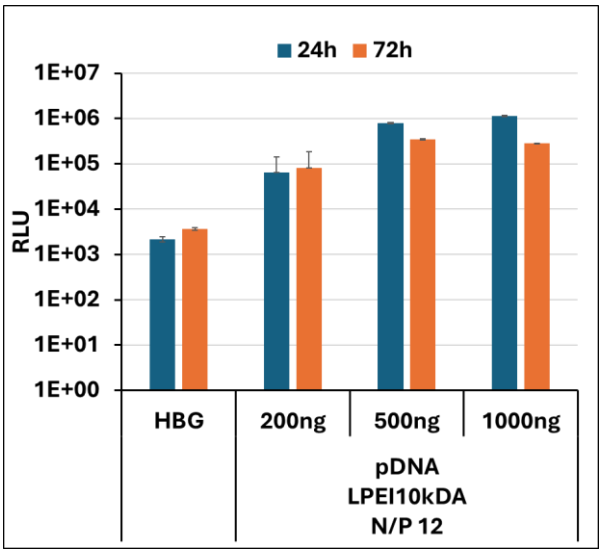

Figure 21: Gaussia luciferase (GLuc) expression from CT26Luc spheroids (day22) transfected with Gluc-pDNA based polyplexes prepared from LPEI 10kDa at N/P ratio of 12. Gluc assay was done at different timepoints after transfection as indicated and luminescence is plotted as RLUs. N=2 i.e. two measurements from one spheroid. Buffer control is plotted as HBG.

Based on these observations from the optimization trial, all subsequent transfection experiments were conducted with an incubation time of 24 hours.

Furthermore, an optimization experiment was set to compare different concentrations of Polyplexes to optimize and evaluate their transfection rate. Additionally, the incubation time of Polyplexes in basal media was doubled to 4 h to identify whether prolonged waiting would affect the transfection efficiency positively. For the experimental layout 5K spheroids were seeded. For the Polyplex formulations, GLuc-pDNA complexed with cLPEI 0,5 N/P 9 were used to test cLPEI´s transfection performance. Transfections were conducted on day 20 and 27 of growth. Per data point 2 spheroids were transfected and measured. Additionally, the spheroids on day 27 were used for the comparison of 2 h vs 4 h waiting time prior to adding complete media and were further measured for cell viability. Resazurin assay was evaluated after the treatment and GloMax® readout. HBG-treated spheroids were used as a control group.

As displayed in Figure A 4**,** different concentrations of GLuc-pDNA were used to assess the transfection rate. While the Polyplexes with GLuc-pDNA 200 ng/well resemble the HBG-treated control group in signal intensity, a higher signal can be seen for the GLuc-pDNA 500 and 1 000 ng/well Polyplexes. This suggests that the Polyplexes with higher

pDNA load achieved a higher transfection rate. The intensity of the GLuc-pDNA 1000 ng/well Polyplexes displayed the best results.

For 2 h vs. 4 h waiting time comparison on day 27 spheroids were divided into two groups. For the first group Polyplexes were added to spheroids in basal media and left to incubate for 2 h before adding complete media, as standard procedure. The spheroids of the second group were left to incubate for 4 h with added Polyplexes in basal media. Moreover, control groups which were only treated with HBG were kept in both groups. To assess the transferability of the Polyplexes different concentrations were tested out. Supernatant of the treated spheroids was harvested 24 h after Polyplex addition. As displayed in Figure 22, for both groups no significant difference in the signals could be observed. When comparing 2 h vs. 4 h waiting time prior to adding complete media, no benefit is discernible in transfectability. The HBG-treated control groups resembled the signals of both incubation times for GLuc-pDNA 200 ng Polyplexes. GLuc-pDNA 500 ng and 1000 ng Polyplexes showed greater signal intensities than the background, with the highest signal coming from the GLuc-pDNA 1000 ng Polyplexes. Although, the highest transfection rate was measured for the GLuc-pDNA 500 ng Polyplexes after 2 h waiting time, the standard deviation of this data point was more elevated compared to the others.

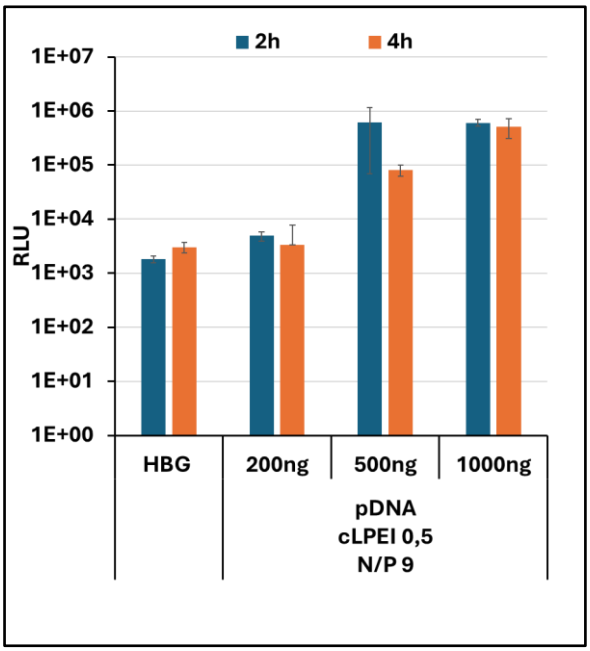

Figure 22: Gaussia luciferase (GLuc) expression from CT26Luc spheroids (day 27) transfected with GLuc-pDNA based Polyplexes prepared from cLPEI polymers at N/P ratio of 9. Three different concentrations of the Polyplex were either

incubated in basal media for 2 h or 4 h before adding complete media to assess the transfection efficiency. HBG buffer treated spheroids were kept as a control group. N=2 spheroids with one measurement per spheroid; readout was done after 24 h treatment.

After transfection the cell viability of both groups was measured via resazurin assay. As shown in Figure A 5, the control groups for both incubation times displayed the greatest signal in cell viability. With increasing Polyplex load decreased cell viability can be seen respectively for both waiting times prior to adding complete media. For the spheroids with 2 h waiting time the cell viability is showing a descent in signal. The 4 h waiting time group displayed similar results with exception for the GLuc-pDNA 500 ng Polyplex. For this resazurin assay no blank as the baseline level was conducted.

The data suggests that with increasing nucleic acid amounts the transfection signal is elevated. Comparing the two waiting times, the data does not demonstrate any significant benefit in waiting 4 h before adding the complete media. On the contrary, the transfection rate and the cell viability for the 2 h waiting time prior to adding complete media exhibited better results across nearly all data points. Overall, due to Polyplexes having a toxic effect on spheroids, cell viability is increasingly compromised at greater nucleic acid concentrations.

For optimization, spheroids on day 16 of growth were used to test transfection kinetics readout approach and comparison of cLPEI with pegylated LPEI. Polyplexes were produced with a concentration of 40 µg/mL of either GLuc-mRNA or GLuc-pDNA complexed with cLPEI or pegylated LPEI. Per Polyplex one spheroid was transfected. To estimate the kinetic rate, 2x 20 µL were collected from each spheroid at five different timepoints (2 h, 4 h, 6 h, 8 h, 24 h) and measured in duplicates. As a control group a HBG-treated spheroid was measured.

Initially, GLuc-mRNA transfections in general showed a faster onset, especially Polyplexes containing cLPEI. However, after 24 h of treatment mRNA Polyplexes produced with pegylated LPEI displayed slightly higher transfection signals. In contrast, GLuc-pDNA exhibited a slower initial transfection rate. After 24 h, however, Polyplexes containing GLuc-pDNA displayed a slightly higher overall transfection signal. Regarding employed

polymers, cLPEI was observed to give the highest overall signal after 24 h treatment, while GLuc-pDNA Polyplexes with pegylated LPEI showed similar results as the mRNA versions.

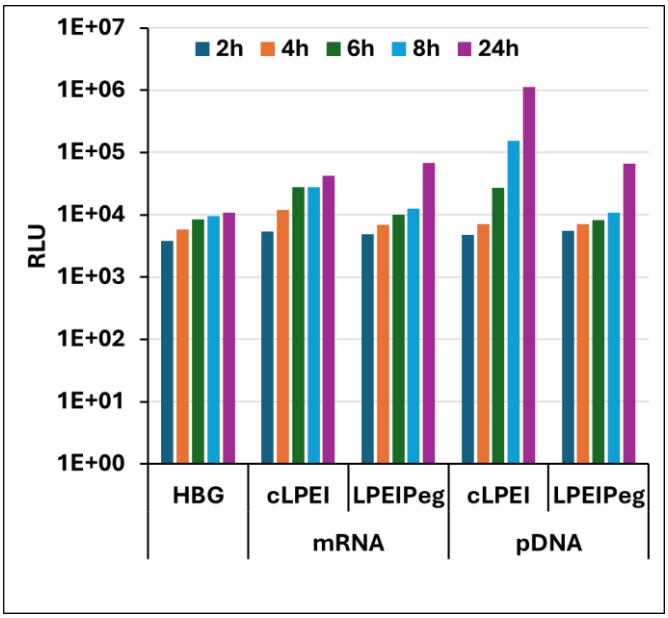

Figure 23: Gaussia luciferase (GLuc) expression kinetics from CT26Luc spheroids (day16) transfected with Gluc-mRNA or Gluc-pDNA based polyplexes prepared from cLPEI or LPEI-PEG polymers at N/P ratio of 12. GLuc assay was done at different timepoints after transfection as indicated and luminescence is plotted as RLUs. N=2 i.e. two measurements from one spheroid. Buffer control is plotted as HBG.

In general, for the CT26Luc cell line the Polyplexes complexed with cLPEI worked slightly better regarding transfections than pegylated LPEI and mRNA initially exhibited faster transfection rates.

8.2 4T1 breast cancer spheroids

8.2.1 Optimization of spheroid formation

4T1-spheroid optimization

The layout of this experiment was designed to observe the growth of both cell lines 4T1 SCR & 4T1 MTHFD1L. Images were captured, and cell viability was assessed on alternate days to monitor their progress. In addition to this, supernatant from designated spheroids was collected, pooled and stored for formate assay on the days: 3, 6, 8, 10, 13, 15, 17, 20, 22, 24, 27, 29, and 31. Furthermore, necrotic core visualization was tested out on day 31 and Polyplexing was optimized for both cell lines. The results of the Polyplexing will be concluded in section 8.2.3. Per cell line, spheroids were seeded at densities of 5K and 10K cells per well.

Figure 24 shows the images captured prior cell viability assay, chronologically separated. As the phase contrast images show, spheroids formed throughout the experiment. Compared to CT26Luc spheroids, the 4T1 cell lines do not form compact spheroids. The cells on the outer shell tend to float relatively freely around the denser core of the spheroids while still being attached. As the spheroids increase in size, the structure becomes progressively looser. This effect was observed to a slightly greater extent for the MTHFD1L cell line. Present fibres in the wells were incorporated into the spheroids, showing a similar behaviour observed for the CT26Luc cell line. Although, the cells are not as strongly attached to themselves or other surfaces.

This phenomenon was observed in both 2D and 3D cell cultures of the 4T1 cancer cell line. The cells exhibit disorganized and highly dynamic cell-cell junctions, which are frequently breaking and re-establishing contacts. Especially in collagen matrix embedded 3D models 4T1 cancer cells displayed significant invasion with single cells and cell aggregates migrating outwards. The high migratory capacity observed in 3D culture may, at least in part, be driven by the dynamic and unstable nature of their cell-cell junctions[46].

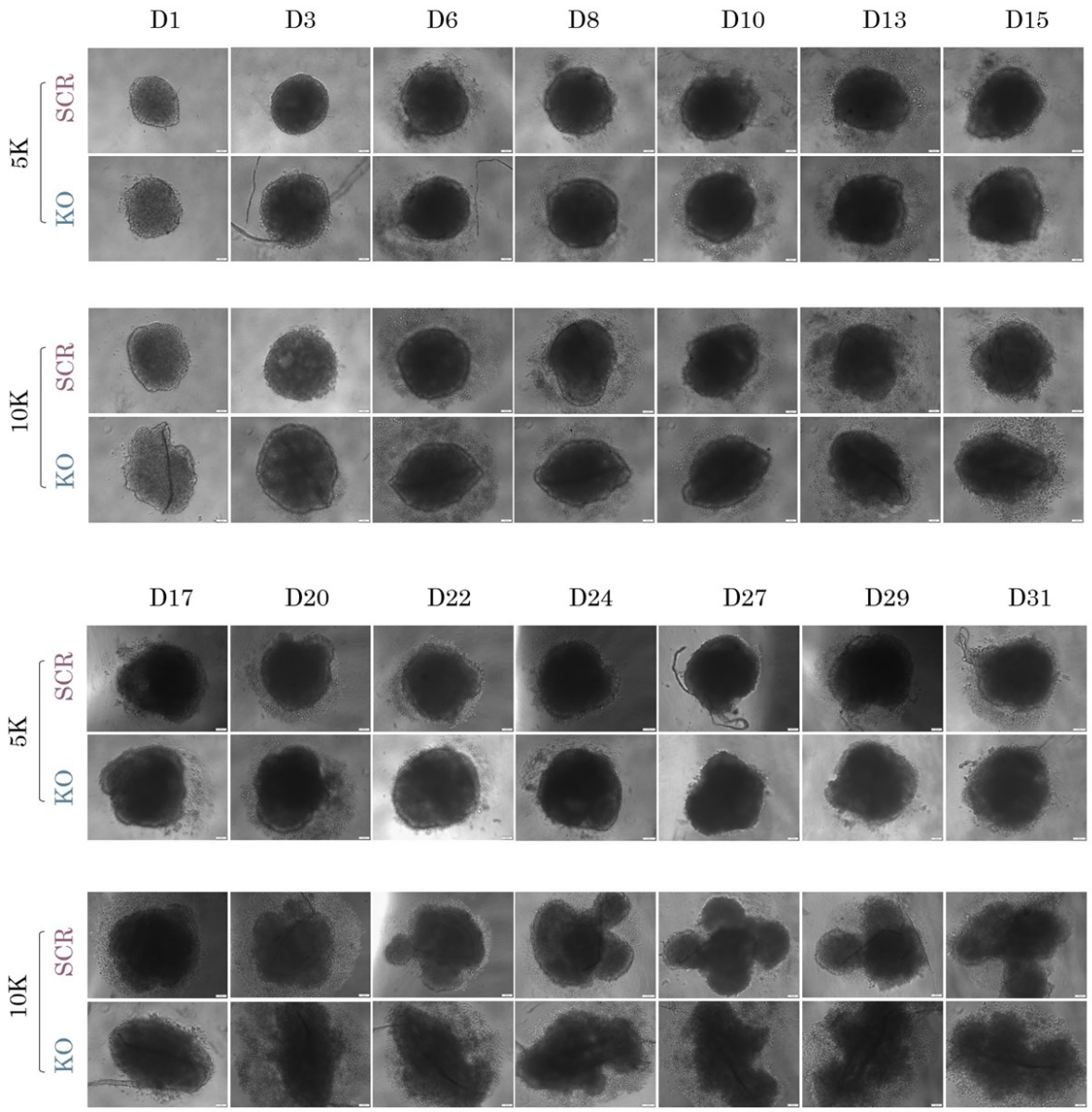

Figure 24: Phase contrast microscopy images of 5K and 10K 4T1 SCR and MTHFD1L (KO) spheroids (n=3) at different durations of growth, as per the indicated timepoints. One replicate is shown out of n=3 spheroids. D=day; automatic exposure time.

The cell viability assay Figure 25 over the time of the experimental layout supports the phase contrast images that the spheroid growth progressed nicely. For better visualization the 5K and 10K cell spheroids are presented in different graphs. Figure 25a shows the cell growth of the 5K cell spheroids. In the beginning both cell lines demonstrated similar growth rates until day 13, then growth began to stagnate for both. Afterwards the MTHFD1L cell line exhibited slightly higher cell viability signals than the

SCR cell line. Additionally, as the spheroids continued to grow, the standard deviation of RFU increased progressively.

For the 10K cell spheroids (Figure 25b), the cell viability of both cell lines was very similar in signal intensity. Starting from day 8 of spheroid growth the measured data points started to exhibit slight stagnation while remaining highly comparable. On the contrary, standard deviation did not increase as much as for the 5K cell spheroids. A drop in signal is notable on day 27 of spheroid growth, which appears to be the only outlier in the dataset.

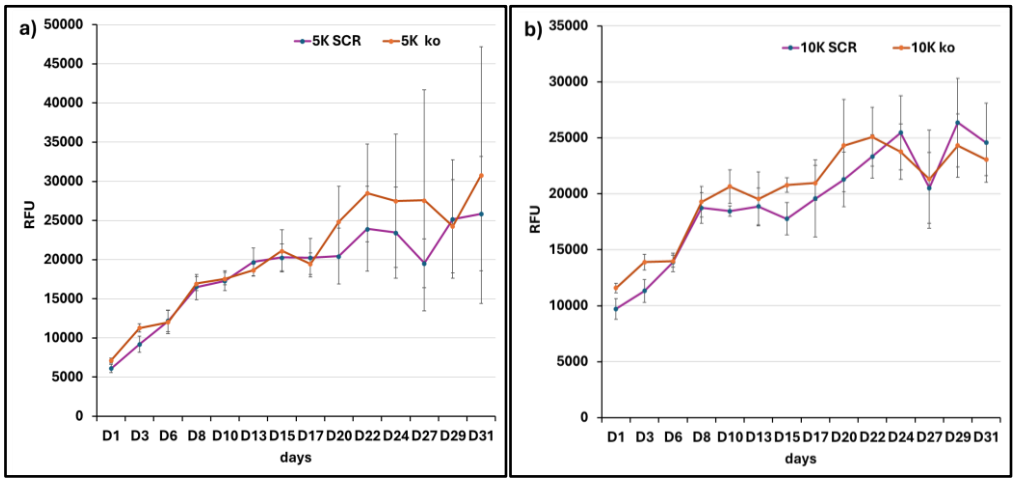

Figure 25: Relative fluorescence signal as RFU through resazurin cell viability assay of 4T1 SCR and MTHFD1L (ko) spheroids. a) 5K spheroids. b) 10K spheroids. N=3 spheroids with one measurement per spheroid.

On day 31 of spheroid growth necrotic core staining and visualization of the SCR and the MTHFD1L was conducted. Figure 26 show the middle perspective of the captured Z-Stacks. A side-by-side comparison of both cell lines aids in distinguishing viable from already apoptotic cells. The loose cells orbiting the dense spheroid core were found to be viable for both cell lines. The most distinguishable difference between both cell lines is the altered morphological structure. Although, phase contrast images appear rather comparable, the MTHFD1L cell line evidently exhibits a notably smaller necrotic core. In contrast, the SCR cell line shows a distinct core of apoptotic cells, resulting in a much higher emitted fluorescent signal.

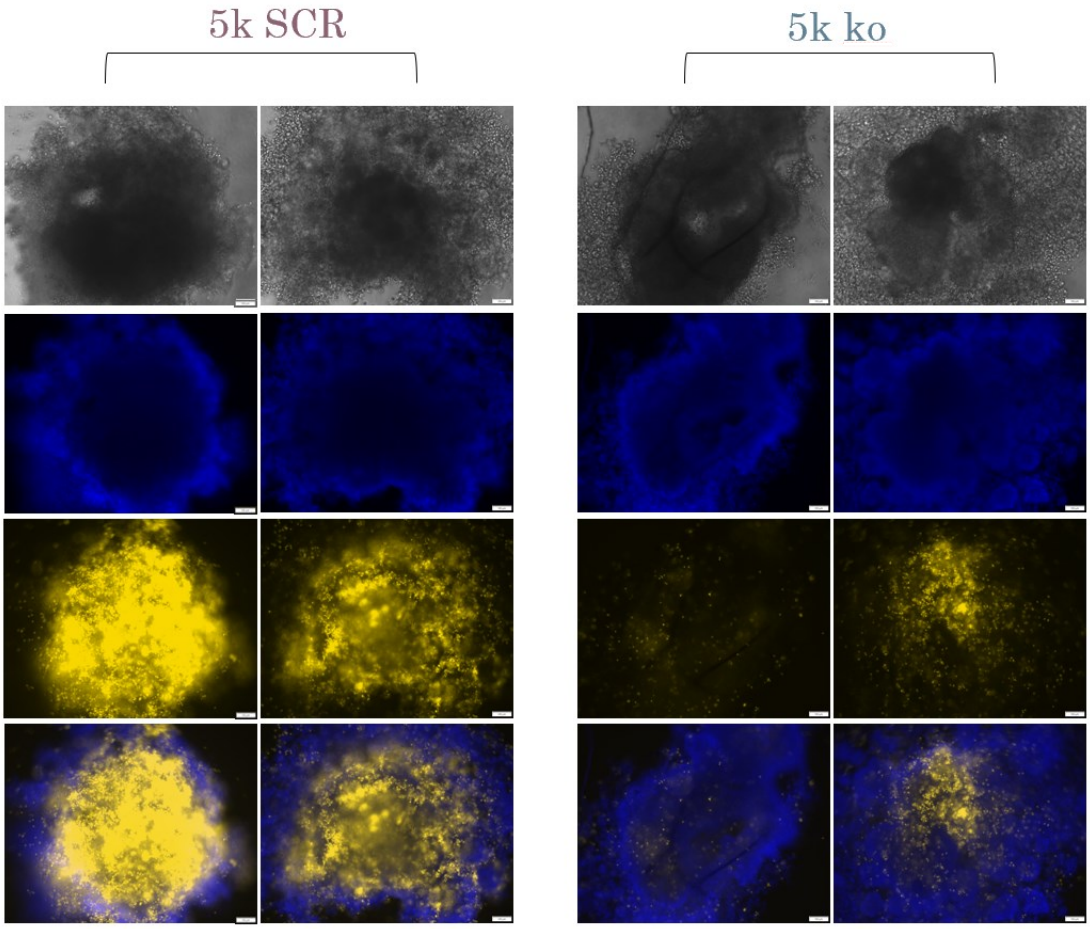

Figure 26: Live/dead staining of 4T1 SCR and MTHFD1L (ko) spheroids (initial seeding amount of 5k cells; n=2 spheroids) via fluorescence microscopy (FLM). Spheroids were stained on day 31. Top row displays the phase contrast microscopy images of the spheroids with Hoechst (conc. 8 µg/mL, exposure time=80 ms, DAPI filter), propidium iodide (conc. 50 µg/mL, exposure time=10 ms, Cy3 filter), and an overlay of both staining's in descending order. 2 h incubation time for the staining solutions.

To assess the format concentration for both cell lines, four designated days of the collected and pooled supernatants were measured (shown in Figure 27). Formate concentration was evaluated for all datapoints and was increasing with spheroid growth. Although, an overall increase in signal intensity is displayed for SCR and MTHFD1L cell line, the initial two data points for both cell lines do not align with the rest.

Contrary to the assumption, that the SCR cell line would produce more formate overflow compared to the MTHFDL cell line, as the knock out of the enzyme disrupts the one-carbon metabolism, the SCR cell line exhibited lower formate concentrations in the supernatant in the first two datapoints[47].

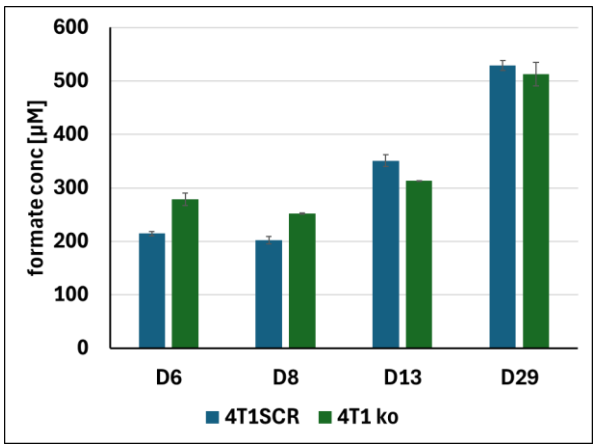

Figure 27: Formate assay evaluation of 4T1 SCR and MTHFD1L (ko) spheroids. Supernatant was collected on the days 6, 8, 13, and 29. Supernatant was pooled from 10 spheroids and measured in triplicates.

8.2.2 Necrotic core visualization

The experiment was designed to observe the spheroid growth of both cell lines and assess the alteration in necrotic core. Per cell line spheroids with a density of 5K cells were seeded. Necrotic core staining was conducted on alternate days as well as cell viability assay. Phase contrast microscopy images were captured prior. The experimental layout was conducted four times in total under identical parameters, with two experiments performed simultaneously in each run. During the first two experiments media change on day 3 was omitted unintentionally, resulting in a deviation of results. Therefore, the results of these two experiments are not presented in this master thesis.

For experiment 3 and 4 no media change was unintentionally left out. The experiments proceeded as per protocol. Spheroids formed and increased in size. As the phase contrast microscopy images show (Figure 28), the spheroid growth progressed rather slowly especially for the SCR cell line. When compared to the optimization experiment, the SCR spheroids did not increase in size significantly. The MTHFD1L cell line began to exhibit loosely floating cells orbiting the denser spheroid core as early as day 6, while this was not observed for the SCR spheroids.

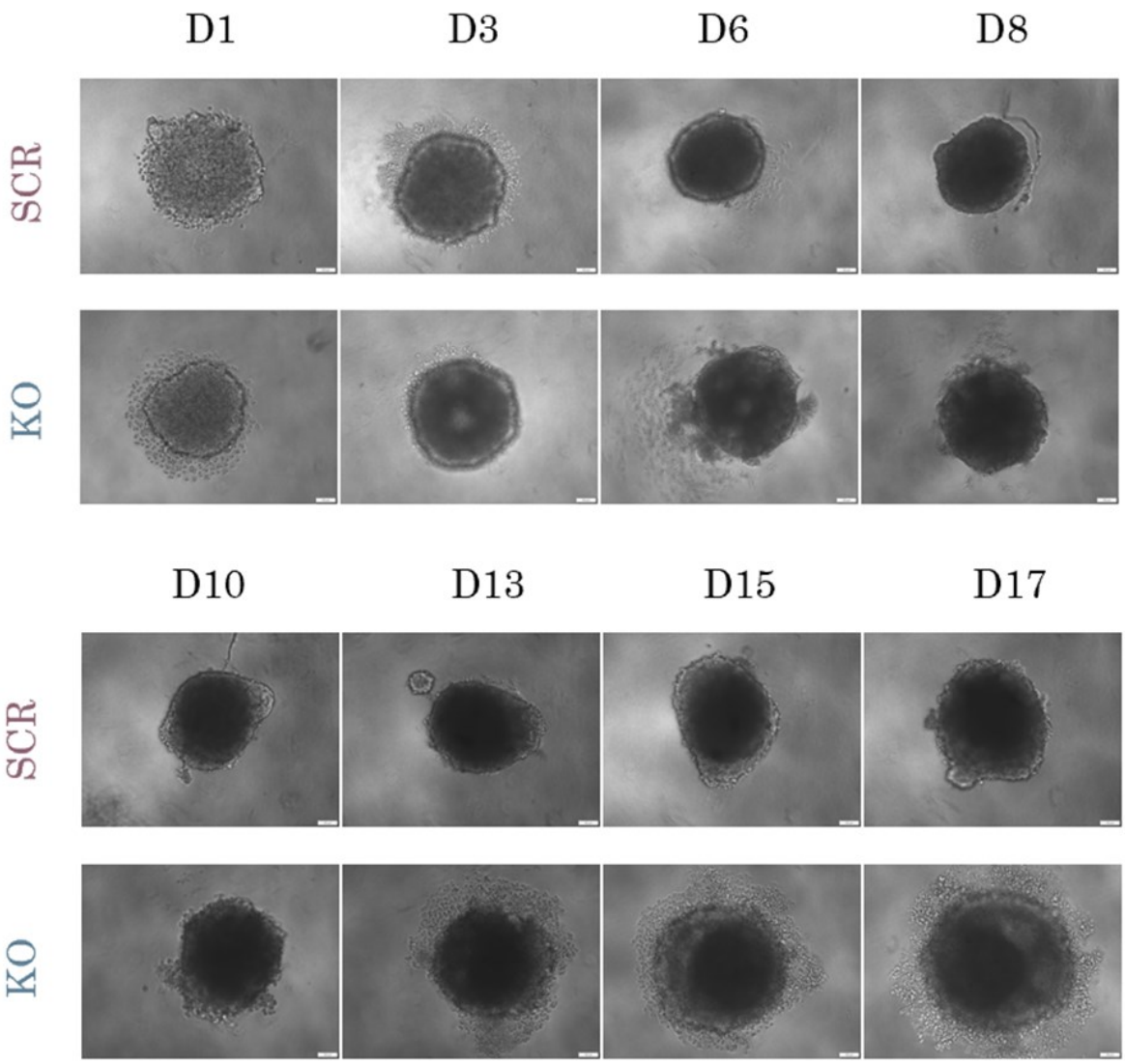

Figure 28: Phase contrast microscopy images of 5K 4T1 SCR and MTHFD1L (KO) spheroids at different durations of growth, as per the indicated timepoints. Images are extracted from experiment 4. One replicate is shown out of n=3 spheroids. D=day; automatic exposure time.

The necrotic core visualizations are displayed in Figure 29. For better comparison, the images of both experiments are put in a vertical stack. Initially, on day 1 no necrotic core was evident. However, on day 3 and onwards an apoptotic centre started to form and increased in size. Both cell lines remained comparable until day 6, showing no significant difference in fluorescent signal and structure prior to that. Nevertheless, the MTHFD1L cell line displayed a distinctly altered structure from day 6 onwards. The necrotic core appeared less evident when compared to the SCR cell line. This distinct variation in morphology highlights a clear difference between the two cell lines, starting already in the

early stages of the experiment. While the SCR spheroids maintained a centrally localized necrotic core, the MTHFD1L cell line displayed the characteristic more scattered growth pattern over time. Additionally, apoptotic cells were scattered throughout the entire spheroid and the signal intensity for the MTHFD1L cell line was not as evident as for the SCR.

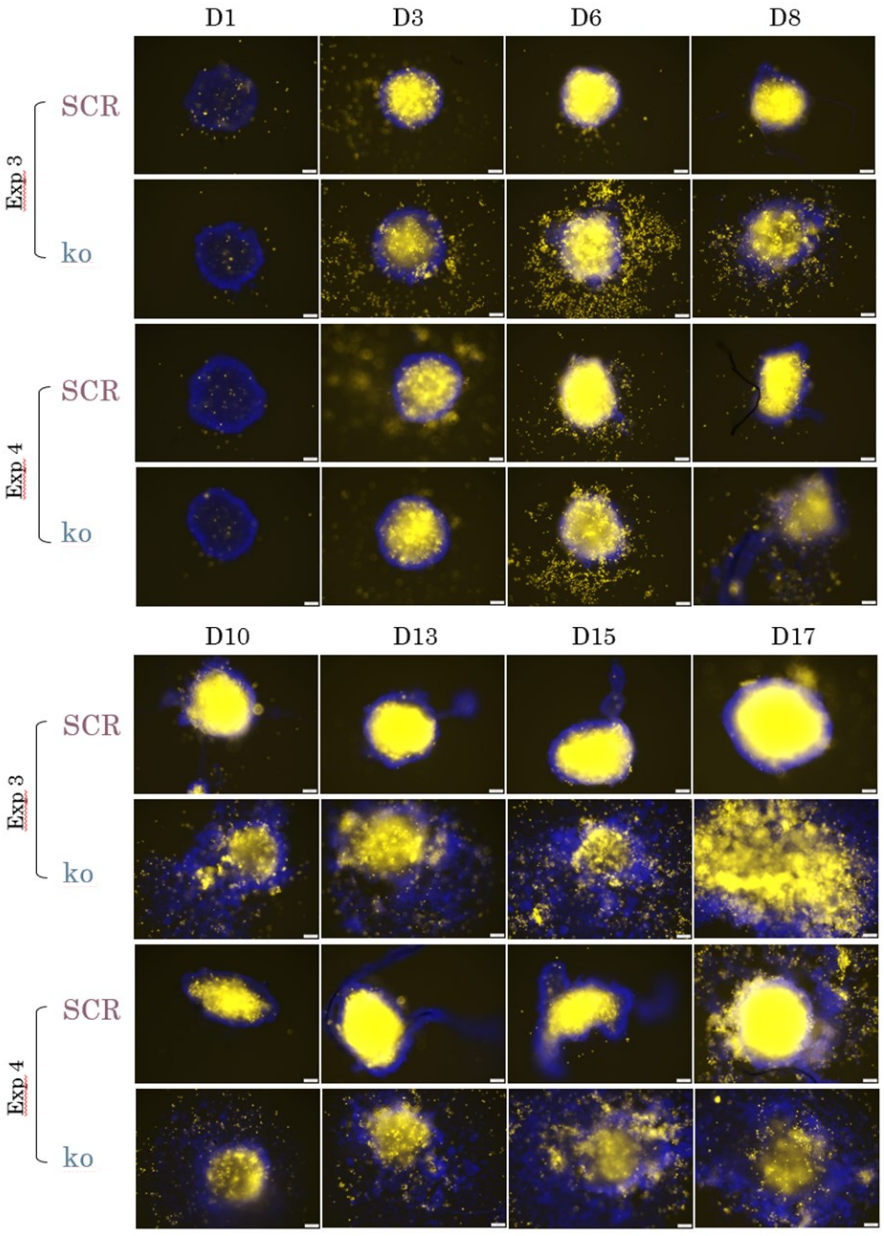

Figure 29: Necrotic core staining of 5K 4T1 SCR and MTHFD1L (KO) spheroids via fluorescence microscopy (FLM). Spheroids of both cell lines were stained with Hoechst and propidium iodide (PI). Images were captured as Z-stacks (exposure time for Hoechst=10 ms with DAPI filter, conc. 8 µg/mL; exposure time for PI=5 ms with Cy3 filter, conc. 50 µg/mL) and the assumed middle perspective was extracted. The shown images show two out of n=4 spheroids. 2 h incubation time for the staining solutions; D=day.

The corresponding cell viability to the spheroids can be seen in Figure 30a for experiment 3 and in Figure 30b for experiment 4. For experiment 3, the two cell lines had relatively comparable initial seeding level. The cell viability signal rose initially and then dropped noticeable on day 13. In contrast, the seeded amount for experiment 4 displayed a greater variation. In addition to this, the measured data points exhibited a highly irregular pattern throughout the experiment. By day 13 the cell viability of the two cell lines dropped to nearly identical intensity. Afterwards, on day 15 an increase in signal intensity was observed in both experiments, with values nearly doubling compared to the previous time point.

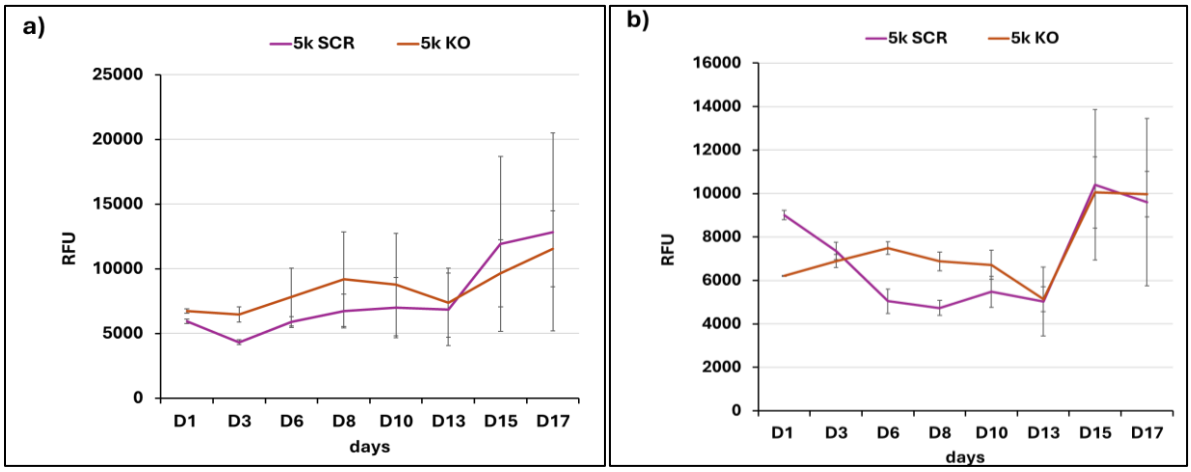

Figure 30: Relative fluorescence signal as RFU through resazurin cell viability assay on 5k 4T1 SCR and MTHFD1L (KO) spheroids. a) cell viability from experiment 3. b) cell viability from experiment 4. N=3 spheroids with one measurement from one spheroid per experiment.

The observed drop in signal intensity on day 13 in experiment 3 and 4 was due to unknown factors. No major incidents occurred during the workflow of the experiment. One possible explanation of these outliers might be the passage number of the cancer cells used. Since the passage number of cells prior to treatment is a crucial factor, it may have influenced viability assays such as the resazurin assay[48].

8.2.3 Transfection of spheroids with mRNA Polyplexes

Optimization

The aim of this experimental design was to evaluate the transfection rate with different Polyplex formulations. For this objective, Polyplexes containing 40µg/mL GLuc-mRNA/ pDNA and cLPEI/ pegylated LPEI were produced. For the cLPEI a N/P ratio of 9 or 12 was aimed. The primary transfection was conducted on day 14. Furthermore, on day 49 a kinetics readout was estimated on to observe the transfection rate in detail. It should be noted that transfection was only conducted on the SCR cell line. After polyplex addition spheroids were incubated in basal media for 2 h before adding complete media, as per standard procedure.

As presented in Figure A 6, the results of the various Polyplex formulations are displayed. For this readout cLPEI had a N/P ratio of 12. Objectively spheroids with 5K and 10K cell density were used. Per each Polyplex a single spheroid was transfected, and data points were obtained by collecting 2x20 µL of supernatant, which was measured in duplicates. The readout was performed after 24 h treatment. To estimate the background noise, blank media was measured and subtracted. The highest transfection rate was observed for the 5K cell spheroids treated with the GLuc-pDNA cLPEI Polyplex mixture. Overall, Polyplexes containing GLuc-pDNA exhibited superior transfection efficiency compared to those formulated with GLuc-mRNA. Moreover, the measured data points for the pegylated LPEI Polyplexes displayed less variability than the cLPEI Polyplexes. The GLuc-mRNA cLPEI Polyplex displayed the lowest signal intensity among all formulations.

4T1 Transfection and cell viability

For this experimental layout spheroids with 5K cells density were seeded. The aim involved the evaluation of transfection rates of cLPEI polyplexes at N/P ratios of 9 and 12 with GLuc-pDNA and GLuc-mRNA for the 4T1 SCR cell line. The treatment dosage of GLuc-mRNA and GLuc-pDNA remained consistent throughout the experiments, i.e.1000 ng per well. Prior and after 24 h treatment phase contrast images were captured. Additionally, after the transfection the cell viability was measured. This was done to estimate the toxic effects Polyplexes might have on the spheroids. Transfections were

conducted on day 8 and 15 of spheroid growth. Additionally, day 8 was reconducted with the same experimental layout to provide supporting data. Per Polyplex 5 spheroids were employed. Moreover, a control group treated with HBG buffer served as comparison.

The left column displays the phase contrast images of the spheroids taken prior to the treatment, while the right column displays same spheroid after 24 h treatment, as shown in Figure 31. In the top row one out of five spheroids from the HBG-treated control group can be seen, followed by GLuc-mRNA and GLuc-pDNA with various N/P ratios. The images for the nucleic acid treated spheroids demonstrate a distinct cell demise.

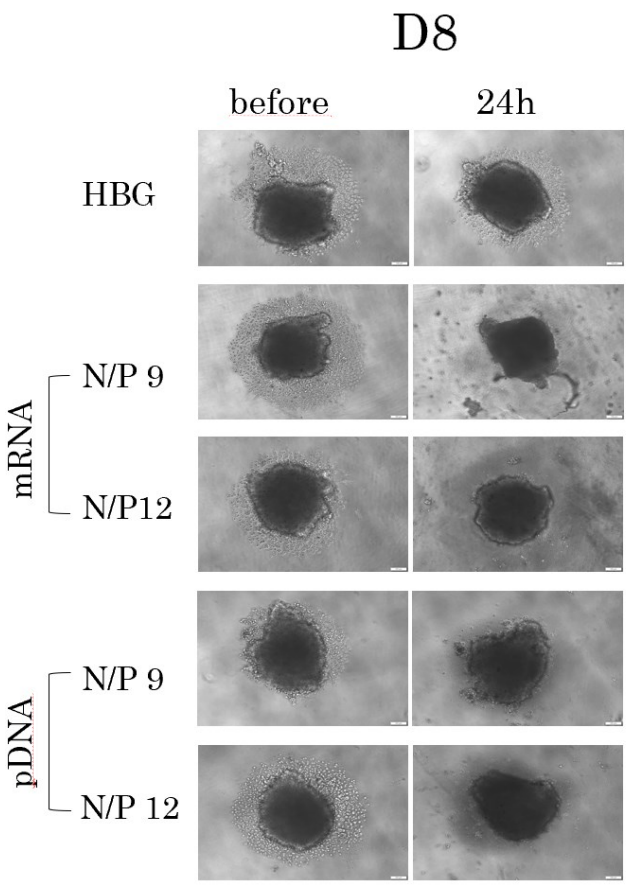

Figure 31:Phase contrast microscopy images of 5K 4T1 SCR spheroids (n=5) on day 8 before and after transfection with Polyplexes containing GLuc-mRNA/pDNA with different N/P ratios: The left column displays the spheroids before transfection and the right column after 24 h treatment. One out of five spheroids is displayed. Automatic exposure time, 10x magnification.

The cell viability of the spheroids 24 h post-transfection is shown in Figure 32a. In comparison to the Polyplex-treated spheroids, the control group exhibited the highest cell viability signal. When comparing GLuc-mRNA to GLuc-pDNA, spheroids showed higher signals for GLuc-pDNA. The highest signal was observed with an N/P ratio of 9 and GLuc-pDNA as nucleic acid. While the lowest cell viability was measured from the Polyplex formulation of GLuc-mRNA and a N/P ratio of 9.

Similar results were obtained from the reconduction of the experiment on day 8 of spheroid growth (Figure A 7). The measured data points support the claim that the produced Polyplex containing GLuc-pDNA with a N/P ratio of 9 exhibited the highest signal intensity among all Polyplexes. GLuc-mRNA with a N/P ratio of 12 displayed the lowest cell viability. Although, the signal was only slightly lesser than for the N/P ratio of 9.

The Glomax® readout displaying the transfection rate is shown in Figure 32b. The HBG-treated control group represents the background signal. While the Polyplexes containing GLuc-pDNA exhibited the highest signal, regardless of the N/P ratio. However, the standard deviation was slightly greater for the N/P of 12. Additionally, both Polyplex formulation with GLuc-mRNA were similar in transfection. Nonetheless, GLuc-mRNA treated spheroids still displayed a lower signal than the GLuc-pDNA treated ones.

Comparably, the reconduction of the Glomax® readout for the second experiment aligns with the previous data (Figure A 8). However, the transfection rates displayed slightly lower intensities for the Polyplexes produced with a N/P ratio of 12 for both nucleic acids.

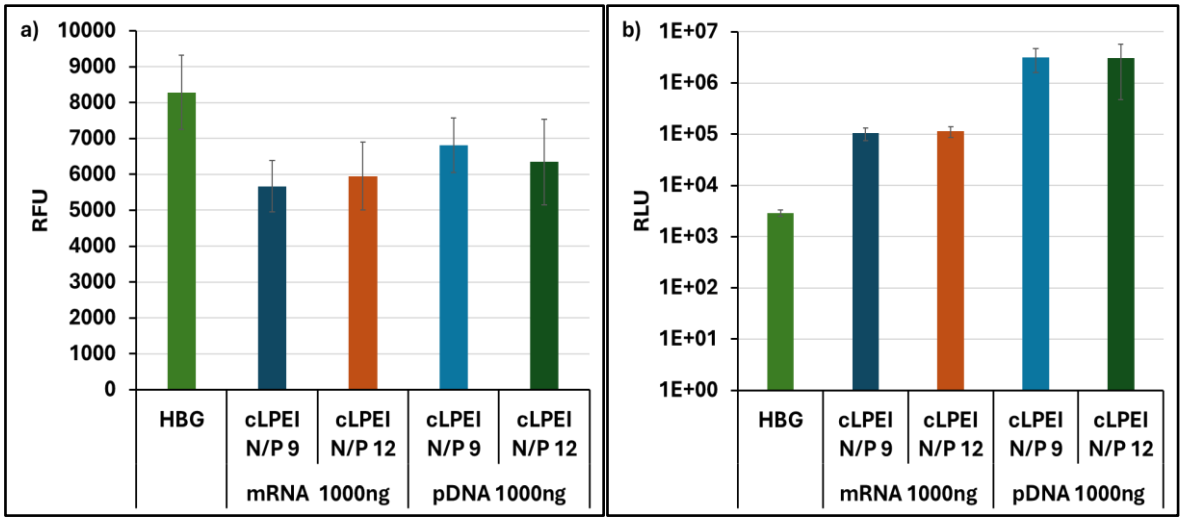

Figure 32: a) Relative fluorescence signal as RFU through resazurin cell viability assay on 5k 4T1 SCR (day 8). N=5. one measurement from one spheroid. b) Gaussia luciferase (GLuc) expression from 4T1 SCR spheroids (day 8) transfected with GLuc-pDNA based and GLuc-mRNA based Polyplexes prepared from cLPEI polymers at N/P ratio of 9 and 12. HBG buffer treated spheroids were kept as a control group. N=5 spheroids with one measurement per spheroid; readout was done after 24 h treatment.

For the transfection on day 15 of spheroid growth the same structure is used to display the phase contrast images (Figure 33). The left column shows the spheroids prior to the treatment and the right column shows them after the treatment of 24 h. The used nucleic acids and N/P ratios are once more shown separately in a vertical stack. As observed previously, the spheroids appear affected by the Polyplexes. The outer cell layer is less distinct, supporting the hypothesis that the polyplexes exert a toxic effect on the cells.

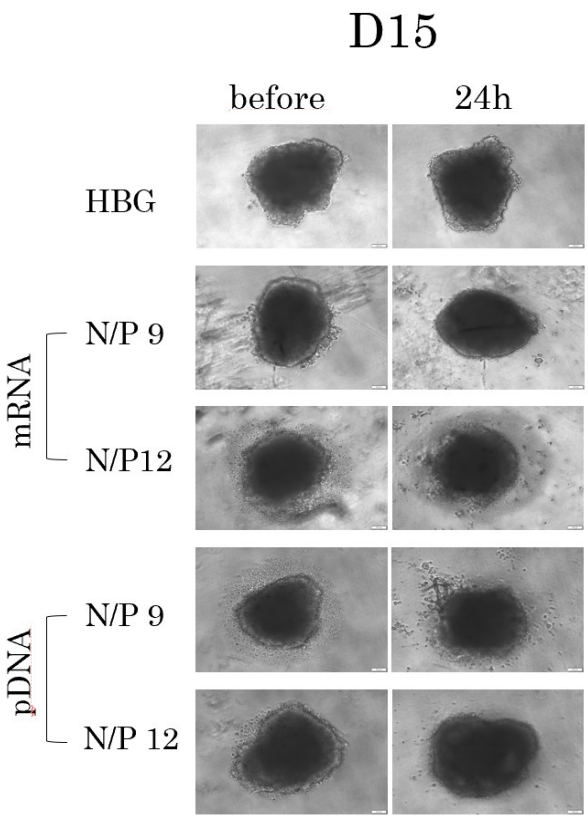

Figure 33: Phase contrast microscopy images of 5K 4T1 SCR spheroids (n=5 spheroids) on day 15 before transfection with Polyplexes containing mRNA/pDNA with different N/P ratios: Used Polyplex formulations are listed on the side beside the belonging spheroid. The left column shows the spheroids before transfection and the right column after 24 h treatment. Automatic exposure time.

For the cell viability, shown in Figure 34a, similar results were obtained as for the experiment on day 8 of growth. Consistent with the previous data, the highest signal was measured for the Polyplex mixture of GLuc-pDNA and a N/P ratio of 9. In contrast, the GLuc-mRNA with a N/P ratio of 12 displayed higher transfection efficiency compared to earlier data. Nonetheless, the signal intensity was still lower compared to the Polyplexes containing GLuc-pDNA. The control group treated with HBG buffer displayed slightly lower cell viability than the GLuc-pDNA Polyplexes. The lowest cell viability was observed in the spheroids treated with GLuc-mRNA at N/P ratio 9. Overall, the most notable difference is the increased standard deviation.

In Figure 34b the transfection efficiency is shown. Once more, the highest signal was observed in Polyplexes formulated with GLuc-pDNA and a N/P ratio of 9. Followed by the signal intensity of the GLuc-pDNA N/P ratio of 12. Polyplexes containing GLuc-mRNA

exhibited comparable transfection efficiency, with the N/P ratio of 9 showing slightly better results than the ratio of 12. Additionally, the control group displayed the lowest signal among all data points.

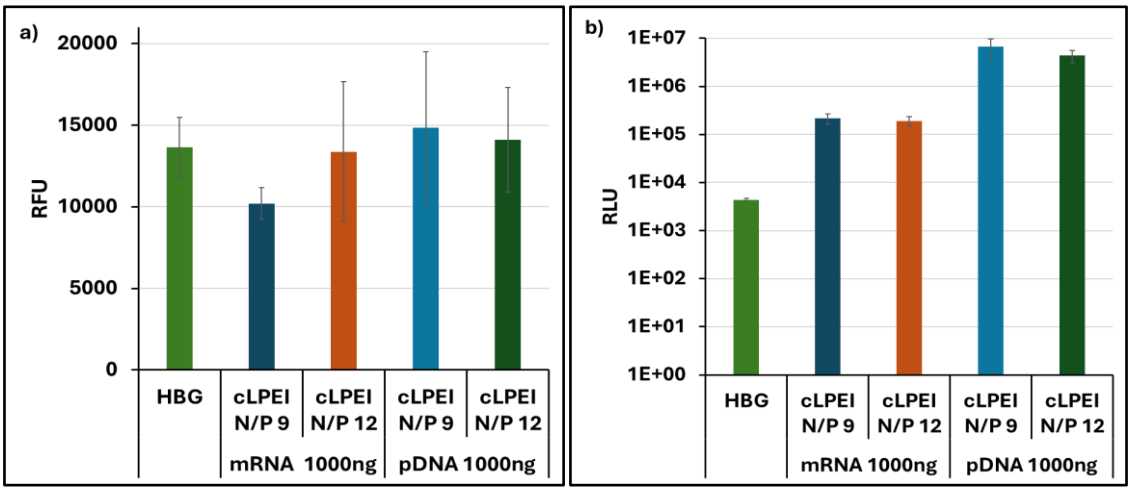

Figure 34: a) Relative fluorescence signal as RFU through resazurin cell viability assay on 5k 4T1 SCR (day 15). N=5. one measurement from one spheroid. b) Gaussia luciferase (GLuc) expression from 4T1 SCR spheroids (day 15) transfected with GLuc-pDNA based and GLuc-mRNA based Polyplexes prepared from cLPEI polymers at N/P ratio of 9 and 12. HBG buffer treated spheroids were kept as a control group. N=5 spheroids with one measurement from one spheroid; readout was done after 24 h treatment.

Interestingly, the Polyplexes produced with GLuc-mRNA showed an overall lower transfection rate and cell viability compared to GLuc-pDNA. This supports the hypothesis that Gluc-mRNA has a notable toxic effect on the spheroids. Additionally, the conducted experiments show that the transfection rate of the Polyplexes is comparable between the different days. One possible explanation might be that the transfection efficiency is bound to increase with higher metabolic activity of the spheroids. However, due to the spheroids growth stagnating at some point as well as the expansion of quiescent and necrotic area, the transfection rate is inevitably expected to plateau.

For the transfection kinetics readout, seeded spheroids with a density of 5K cells were employed. Per Polyplex (GLuc-pDNA/-mRNA conc. 1000 ng/mL) a single spheroid was transfected. The best transfection efficiency was measured for the GLuc-pDNA pegylated LPEI formulation after 48 h. In general, the signals increased with longer incubation time. As demonstrated in Figure 35, GLuc-mRNA exhibited higher signals initially compared to

GLuc-pDNA. Nonetheless, GLuc-pDNA ultimately exhibited better transfection rates after 24 h. When comparing polymers, in this setting pegylated LPEI showed slightly better results than cLPEI. For control group, one spheroid treated with HBG buffer was analysed.

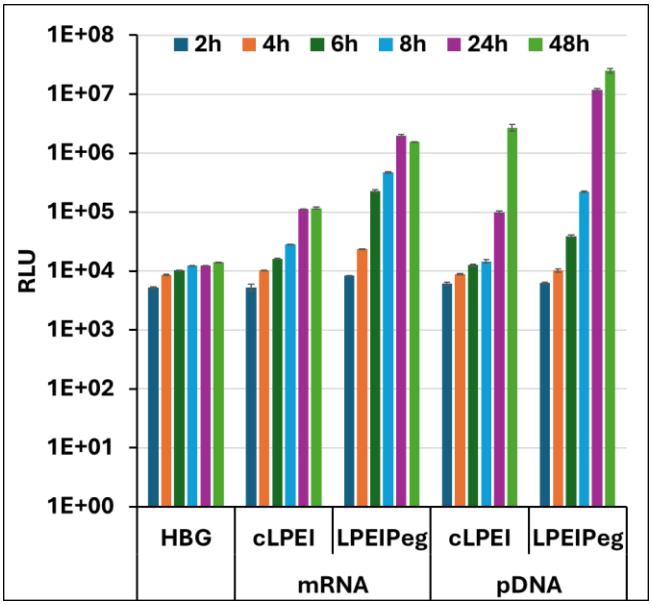

Figure 35: Gaussia luciferase (GLuc) expression kinetics from 5K 4T1SCR spheroids (day 49) transfected with GLuc-mRNA or GLuc-pDNA based polyplexes prepared from cLPEI or LPEI-PEG polymers at N/P ratio of 12. GLuc assay was done at different timepoints after transfection as indicated and luminescence is plotted as RLUs. N=2 i.e. two measurements from one spheroid. Buffer control is plotted as HBG.

9 Conclusion

CT26Luc cancer cell line consistently formed successfully compact and round spheroids. Notably, the necrotic core was already established by the second day of growth and continued to expand further. Moreover, visualization of the necrotic core via FLM with Hoechst and PI dyes proved highly effective. Formate detection of the spheroid supernatant was successful. The measured formate concentrations ranged from approximately 50 µM on day 4 to nearly 250 µM on day 16. However, the exact metabolic pathway for formate overflow remains unclear, as no further metabolic studies were conducted. Regarding Oxaliplatin treatment of CT26Luc spheroids, the findings of this master thesis suggest that, besides the used concentration and incubation time, the timing of administration also plays a crucial role in effective treatment. Spheroids treated on day 6 exhibited the highest viability and were the least affected by Oxaliplatin compared to the other days. In transfection experiments, GLuc-mRNA showed faster onset of signal, whereas GLuc-pDNA achieved overall higher transfectability. The optimal transfection rate was reached within 24 hours, and no significant difference was observed between adding complete media after 2 hours versus 4 hours of Polyplex incubation. Among the tested polymers, cLPEI-based Polyplexes displayed superior transfection rates in the CT26Luc cell line when compared to pegylated LPEI.

Compared to the CT26Luc spheroids, the 4T1 SCR and MTHFD1L-knocked down cell lines formed less compact spheroids, characterized by loosely attached cell aggregates surrounding a denser core. This observation was particularly pronounced in the MTHFD1L-knocked down cell line, which displayed a more dispersed morphology with a higher amount of loose cells as spheroid size increased. Similar to the CT26Luc cell line, the necrotic core in the 4T1 spheroids became evident by day 3. However, its localization, size and structural organisation differed in the MTHFD1L-knocked down compared to the SCR cell line. In the MTHFD1L spheroids, the necrotic core emerged more scattered and less evident compared to the SCR counterpart. The formate detection for both cell lines was conducted simultaneously with concentration ranges from around 200 µM on day 6 to nearly 520 µM on day 29 for the 4T1 SCR spheroids, and from approximately 280 µM to around 510 µM for the 4T1 MTHFD1L spheroids at the corresponding days. Consistent with the observation in CT26Luc spheroids, the best transfectability for 4T1 SCR

spheroids was achieved after 24 hours with GLuc-mRNA displaying more rapid initial signal. GLuc-pDNA yielded again in overall superior transfection efficiency. In contrast, Polyplexes containing pegylated LPEI as polymer demonstrated higher transfectability than cLPEI formulated Polyplexes. Among cLPEI-based formulations, Polyplexes with a N/P ratio of 9 and GLuc-pDNA displayed the best transfection rates while maintaining the highest cell viability.

10 References

(1) *Global cancer burden growing, amidst mounting need for services*. https://www.who.int/news/item/01-02-2024-global-cancer-burden-growing--amidst-mounting-need-for-services (accessed 2024-12-30).

(2) Hanahan, D. Hallmarks of Cancer: New Dimensions. *Cancer Discov* **2022**, *12* (1), 31–46. https://doi.org/10.1158/2159-8290.CD-21-1059.

(3) You, M.; Xie, Z.; Zhang, N.; Zhang, Y.; Xiao, D.; Liu, S.; Zhuang, W.; Li, L.; Tao, Y. Signaling Pathways in Cancer Metabolism: Mechanisms and Therapeutic Targets. *Sig Transduct Target Ther* **2023**, *8* (1), 1–27. https://doi.org/10.1038/s41392-023-01442-3.

(4) Martínez-Reyes, I.; Chandel, N. S. Cancer Metabolism: Looking Forward. *Nat Rev Cancer* **2021**, *21* (10), 669–680. https://doi.org/10.1038/s41568-021-00378-6.

(5) Pietzke, M.; Meiser, J.; Vazquez, A. Formate Metabolism in Health and Disease. *Molecular Metabolism* **2020**, *33*, 23–37. https://doi.org/10.1016/j.molmet.2019.05.012.

(6) Zhu, Z.; Leung, G. K. K. More Than a Metabolic Enzyme: MTHFD2 as a Novel Target for Anticancer Therapy? *Front. Oncol.* **2020**, *10*. https://doi.org/10.3389/fonc.2020.00658.

(7) Stoffel, E. M.; Murphy, C. C. Epidemiology and Mechanisms of the Increasing Incidence of Colon and Rectal Cancers in Young Adults. *Gastroenterology* **2020**, *158* (2), 341–353. https://doi.org/10.1053/j.gastro.2019.07.055.

(8) Menon, G.; Recio-Boiles, A.; Lotfollahzadeh, S.; Cagir, B. Colon Cancer. In *StatPearls*; StatPearls Publishing: Treasure Island (FL), 2024.

(9) Huang, Z.; Yang, M. Molecular Network of Colorectal Cancer and Current Therapeutic Options. *Front. Oncol.* **2022**, *12*. https://doi.org/10.3389/fonc.2022.852927.

(10) Schmitt, M.; Greten, F. R. The Inflammatory Pathogenesis of Colorectal Cancer. *Nat Rev Immunol* **2021**, *21* (10), 653–667. https://doi.org/10.1038/s41577-021-00534-x.

(11) Olson, B.; Li, Y.; Lin, Y.; Liu, E. T.; Patnaik, A. Mouse Models for Cancer Immunotherapy Research. *Cancer Discovery* **2018**, *8* (11), 1358–1365. https://doi.org/10.1158/2159-8290.CD-18-0044.

(12) Narumi, K.; Udagawa, T.; Kondoh, A.; Kobayashi, A.; Hara, H.; Ikarashi, Y.; Ohnami, S.; Takeshita, F.; Ochiya, T.; Okada, T.; Yamagishi, M.; Yoshida, T.; Aoki, K. In Vivo Delivery of Interferon-α Gene Enhances Tumor Immunity and Suppresses Immunotolerance in Reconstituted Lymphopenic Hosts. *Gene Ther* **2012**, *19* (1), 34–48. https://doi.org/10.1038/gt.2011.73.

(13) *Breast cancer*. https://www.who.int/news-room/fact-sheets/detail/breast-cancer (accessed 2025-01-01).

(14) Løyland, B.; Sandbekken, I. H.; Grov, E. K.; Utne, I. Causes and Risk Factors of Breast Cancer, What Do We Know for Sure? An Evidence Synthesis of Systematic Reviews and Meta-Analyses. *Cancers* **2024**, *16* (8), 1583. https://doi.org/10.3390/cancers16081583.

(15) Turner, K. M.; Yeo, S. K.; Holm, T. M.; Shaughnessy, E.; Guan, J.-L. Heterogeneity within Molecular Subtypes of Breast Cancer. *American Journal of Physiology-Cell Physiology* **2021**, *321* (2), C343–C354. https://doi.org/10.1152/ajpcell.00109.2021.

(16) Kaur, P.; Nagaraja, G. M.; Zheng, H.; Gizachew, D.; Galukande, M.; Krishnan, S.; Asea, A. A Mouse Model for Triple-Negative Breast Cancer Tumor-Initiating Cells (TNBC-TICs) Exhibits Similar Aggressive Phenotype to the Human Disease. *BMC Cancer* **2012**, *12* (1), 120. https://doi.org/10.1186/1471-2407-12-120.
(17) Rajaratinam, H.; Rasudin, N. S.; Safuan, S.; Abdullah, N. A.; Mokhtar, N. F.; Mohd Fuad, W. E. Passage Number of 4T1 Cells Influences the Development of Tumour and the Progression of Metastasis in 4T1 Orthotopic Mice. *Malays J Med Sci* **2022**, *29* (3), 30–42. https://doi.org/10.21315/mjms2022.29.3.4.
(18) Kiweler, N.; Delbrouck, C.; Neises, L.; Pozdeev, V.; Soriano-Baguet, L.; Xiang, F.; Benzarti, M.; Haase, L.; Schmoetten, M.; Jaeger, C.; Noman, M.; Vazquez, A.; Janji, B.; Dittmar, G.; Brenner, D.; Letellier, E.; Meiser, J. Mitochondrial One-Carbon Flux Has a Growth-Independent Role in Promoting Breast Cancer Metastasis. In Review July 12, 2021. https://doi.org/10.21203/rs.3.rs-639444/v1.
(19) Chitturi Suryaprakash, R. T.; Kujan, O.; Shearston, K.; Farah, C. S. Three-Dimensional Cell Culture Models to Investigate Oral Carcinogenesis: A Scoping Review. *IJMS* **2020**, *21* (24), 9520. https://doi.org/10.3390/ijms21249520.
(20) Cacciamali, A.; Villa, R.; Dotti, S. 3D Cell Cultures: Evolution of an Ancient Tool for New Applications. *Front. Physiol.* **2022**, *13*, 836480. https://doi.org/10.3389/fphys.2022.836480.
(21) Bédard, P.; Gauvin, S.; Ferland, K.; Caneparo, C.; Pellerin, È.; Chabaud, S.; Bolduc, S. Innovative Human Three-Dimensional Tissue-Engineered Models as an Alternative to Animal Testing. *Bioengineering* **2020**, *7* (3), 115. https://doi.org/10.3390/bioengineering7030115.
(22) Jubelin, C.; Muñoz-Garcia, J.; Griscom, L.; Cochonneau, D.; Ollivier, E.; Heymann, M.-F.; Vallette, F. M.; Oliver, L.; Heymann, D. Three-Dimensional in Vitro Culture Models in Oncology Research. *Cell Biosci* **2022**, *12* (1), 155. https://doi.org/10.1186/s13578-022-00887-3.
(23) Drost, J.; Clevers, H. Organoids in Cancer Research. *Nat Rev Cancer* **2018**, *18* (7), 407–418. https://doi.org/10.1038/s41568-018-0007-6.
(24) Yi, H.-G.; Jeong, Y. H.; Kim, Y.; Choi, Y.-J.; Moon, H. E.; Park, S. H.; Kang, K. S.; Bae, M.; Jang, J.; Youn, H.; Paek, S. H.; Cho, D.-W. A Bioprinted Human-Glioblastoma-on-a-Chip for the Identification of Patient-Specific Responses to Chemoradiotherapy. *Nat Biomed Eng* **2019**, *3* (7), 509–519. https://doi.org/10.1038/s41551-019-0363-x.
(25) Nunes, A. S.; Barros, A. S.; Costa, E. C.; Moreira, A. F.; Correia, I. J. 3D Tumor Spheroids as in Vitro Models to Mimic in Vivo Human Solid Tumors Resistance to Therapeutic Drugs. *Biotech & Bioengineering* **2019**, *116* (1), 206–226. https://doi.org/10.1002/bit.26845.
(26) Patel, T.; Jain, N. Multicellular Tumor Spheroids: A Convenient in Vitro Model for Translational Cancer Research. *Life Sciences* **2024**, *358*, 123184. https://doi.org/10.1016/j.lfs.2024.123184.
(27) El Harane, S.; Zidi, B.; El Harane, N.; Krause, K.-H.; Matthes, T.; Preynat-Seauve, O. Cancer Spheroids and Organoids as Novel Tools for Research and Therapy: State of the Art and Challenges to Guide Precision Medicine. *Cells* **2023**, *12* (7), 1001. https://doi.org/10.3390/cells12071001.
(28) Lin, R.; Chang, H. Recent Advances in Three-dimensional Multicellular Spheroid Culture for Biomedical Research. *Biotechnology Journal* **2008**, *3* (9–10), 1172–1184. https://doi.org/10.1002/biot.200700228.

(29) Han, S. J.; Kwon, S.; Kim, K. S. Challenges of Applying Multicellular Tumor Spheroids in Preclinical Phase. *Cancer Cell International* **2021**, *21* (1), 152. https://doi.org/10.1186/s12935-021-01853-8.
(30) *Characterization of the physical properties of tumor-derived spheroids reveals critical insights for pre-clinical studies | Scientific Reports*. https://www.nature.com/articles/s41598-019-43090-0 (accessed 2025-01-04).
(31) Karsch-Bluman, A.; Feiglin, A.; Arbib, E.; Stern, T.; Shoval, H.; Schwob, O.; Berger, M.; Benny, O. Tissue Necrosis and Its Role in Cancer Progression. *Oncogene* **2019**, *38* (11), 1920–1935. https://doi.org/10.1038/s41388-018-0555-y.
(32) Huang, Y.; Wang, S.; Guo, Q.; Kessel, S.; Rubinoff, I.; Chan, L. L.-Y.; Li, P.; Liu, Y.; Qiu, J.; Zhou, C. Optical Coherence Tomography Detects Necrotic Regions and Volumetrically Quantifies Multicellular Tumor Spheroids. *Cancer Research* **2017**, *77* (21), 6011–6020. https://doi.org/10.1158/0008-5472.CAN-17-0821.
(33) Abd El-Sadek, I.; Morishita, R.; Mori, T.; Makita, S.; Mukherjee, P.; Matsusaka, S.; Yasuno, Y. Label-Free Visualization and Quantification of the Drug-Type-Dependent Response of Tumor Spheroids by Dynamic Optical Coherence Tomography. *Sci Rep* **2024**, *14* (1), 3366. https://doi.org/10.1038/s41598-024-53171-4.
(34) Yakavets, I.; Francois, A.; Benoit, A.; Merlin, J.-L.; Bezdetnaya, L.; Vogin, G. Advanced Co-Culture 3D Breast Cancer Model for Investigation of Fibrosis Induced by External Stimuli: Optimization Study. *Sci Rep* **2020**, *10* (1), 21273. https://doi.org/10.1038/s41598-020-78087-7.
(35) Mittler, F.; Obeïd, P.; Rulina, A. V.; Haguet, V.; Gidrol, X.; Balakirev, M. Y. High-Content Monitoring of Drug Effects in a 3D Spheroid Model. *Front. Oncol.* **2017**, *7*, 293. https://doi.org/10.3389/fonc.2017.00293.
(36) Dettin, M.; Sieni, E.; Zamuner, A.; Marino, R.; Sgarbossa, P.; Lucibello, M.; Tosi, A. L.; Keller, F.; Campana, L. G.; Signori, E. A Novel 3D Scaffold for Cell Growth to Assess Electroporation Efficacy. *Cells* **2019**, *8* (11), 1470. https://doi.org/10.3390/cells8111470.
(37) Sayed, N.; Allawadhi, P.; Khurana, A.; Singh, V.; Navik, U.; Pasumarthi, S. K.; Khurana, I.; Banothu, A. K.; Weiskirchen, R.; Bharani, K. K. Gene Therapy: Comprehensive Overview and Therapeutic Applications. *Life Sciences* **2022**, *294*, 120375. https://doi.org/10.1016/j.lfs.2022.120375.
(38) Van Zundert, I.; Fortuni, B.; Rocha, S. From 2D to 3D Cancer Cell Models—The Enigmas of Drug Delivery Research. *Nanomaterials* **2020**, *10* (11), 2236. https://doi.org/10.3390/nano10112236.
(39) Han, M.; Bae, Y.; Nishiyama, N.; Miyata, K.; Oba, M.; Kataoka, K. Transfection Study Using Multicellular Tumor Spheroids for Screening Non-Viral Polymeric Gene Vectors with Low Cytotoxicity and High Transfection Efficiencies. *Journal of Controlled Release* **2007**, *121* (1–2), 38–48. https://doi.org/10.1016/j.jconrel.2007.05.012.
(40) Zakeri, A.; Kouhbanani, M. A. J.; Beheshtkhoo, N.; Beigi, V.; Mousavi, S. M.; Hashemi, S. A. R.; Karimi Zade, A.; Amani, A. M.; Savardashtaki, A.; Mirzaei, E.; Jahandideh, S.; Movahedpour, A. Polyethylenimine-Based Nanocarriers in Co-Delivery of Drug and Gene: A Developing Horizon. *Nano Rev Exp* **2018**, *9* (1), 1488497. https://doi.org/10.1080/20022727.2018.1488497.
(41) Fus-Kujawa, A.; Prus, P.; Bajdak-Rusinek, K.; Teper, P.; Gawron, K.; Kowalczuk, A.; Sieron, A. L. An Overview of Methods and Tools for Transfection of Eukaryotic Cells

in Vitro. *Front Bioeng Biotechnol* **2021**, *9*, 701031. https://doi.org/10.3389/fbioe.2021.701031.
(42) Nakajima, Y.; Ohmiya, Y. Bioluminescence Assays: Multicolor Luciferase Assay, Secreted Luciferase Assay and Imaging Luciferase Assay. *Expert Opinion on Drug Discovery* **2010**, *5* (9), 835–849. https://doi.org/10.1517/17460441.2010.506213.
(43) Stoddart, M. J. Cell Viability Assays: Introduction. In *Mammalian Cell Viability*; Stoddart, M. J., Ed.; Methods in Molecular Biology; Humana Press: Totowa, NJ, 2011; Vol. 740, pp 1–6. https://doi.org/10.1007/978-1-61779-108-6_1.
(44) Petiti, J.; Revel, L.; Divieto, C. Standard Operating Procedure to Optimize Resazurin-Based Viability Assays. *Biosensors* **2024**, *14* (4), 156. https://doi.org/10.3390/bios14040156.
(45) Ivanov, D. P.; Parker, T. L.; Walker, D. A.; Alexander, C.; Ashford, M. B.; Gellert, P. R.; Garnett, M. C. Multiplexing Spheroid Volume, Resazurin and Acid Phosphatase Viability Assays for High-Throughput Screening of Tumour Spheroids and Stem Cell Neurospheres. *PLOS ONE* **2014**, *9* (8), e103817. https://doi.org/10.1371/journal.pone.0103817.
(46) Herndon, M. E.; Ayers, M.; Gibson-Corley, K. N.; Wendt, M. K.; Wallrath, L. L.; Henry, M. D.; Stipp, C. S. The Highly Metastatic 4T1 Breast Carcinoma Model Possesses Features of a Hybrid Epithelial/Mesenchymal Phenotype. *Disease Models & Mechanisms* **2024**, *17* (9), dmm050771. https://doi.org/10.1242/dmm.050771.
(47) Meiser, J.; Schuster, A.; Pietzke, M.; Vande Voorde, J.; Athineos, D.; Oizel, K.; Burgos-Barragan, G.; Wit, N.; Dhayade, S.; Morton, J. P.; Dornier, E.; Sumpton, D.; Mackay, G. M.; Blyth, K.; Patel, K. J.; Niclou, S. P.; Vazquez, A. Increased Formate Overflow Is a Hallmark of Oxidative Cancer. *Nat Commun* **2018**, *9* (1), 1368. https://doi.org/10.1038/s41467-018-03777-w.
(48) Lavogina, D.; Lust, H.; Tahk, M.-J.; Laasfeld, T.; Vellama, H.; Nasirova, N.; Vardja, M.; Eskla, K.-L.; Salumets, A.; Rinken, A.; Jaal, J. Revisiting the Resazurin-Based Sensing of Cellular Viability: Widening the Application Horizon. *Biosensors (Basel)* **2022**, *12* (4), 196. https://doi.org/10.3390/bios12040196.

11 List of figures

12 List of Appendix figures

13 List of tables

14 Appendix

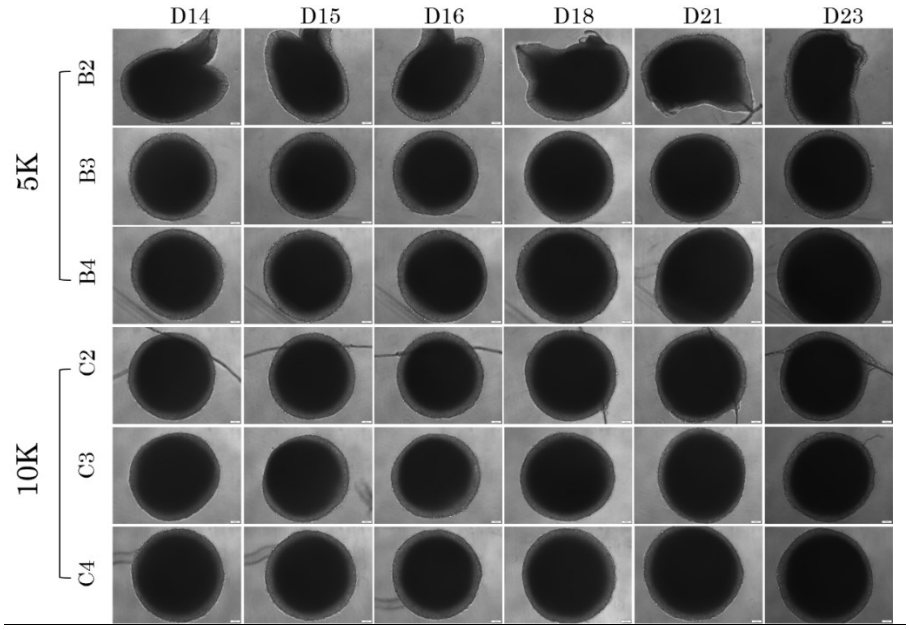

Figure A 1: Phase contrast microscopy images of CT26Luc spheroids from two cell numbers (5K and 10K) at different durations of growth, as per the indicated timepoints. Three replicates (labelled with their well numbers) are shown from n=5 spheroids. D=day; images with automatic exposure, 10x magnification, scale bar size: 100 µm.

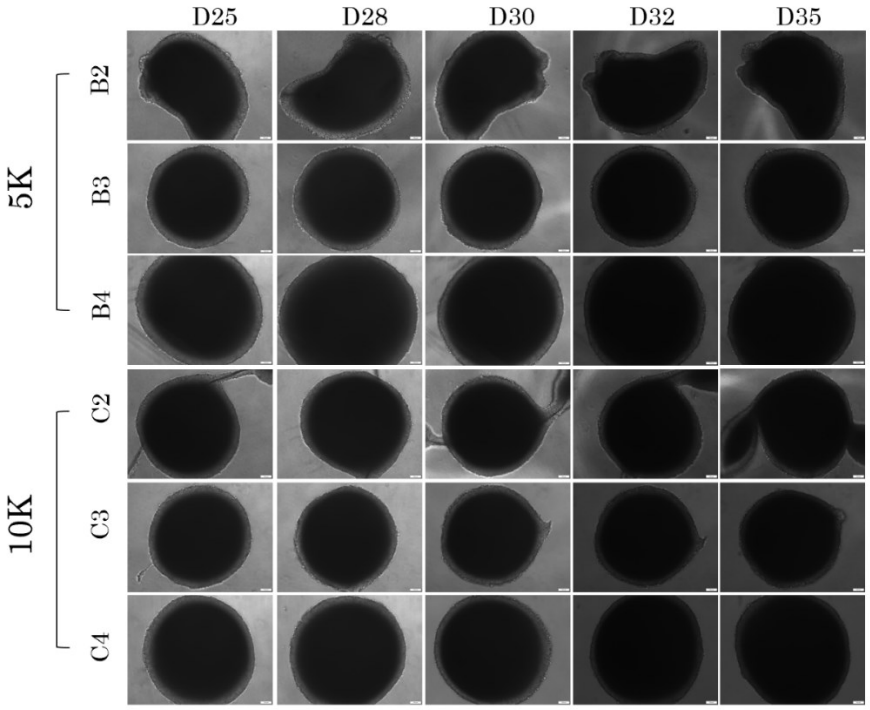

Figure A 2: Phase contrast microscopy images of CT26Luc spheroids from two cell numbers (5K and 10K) at different durations of growth, as per the indicated timepoints. Three replicates (labelled with their well numbers) are shown from n=5 spheroids. D=day; images with automatic exposure, 10x magnification, scale bar size: 100 µm.

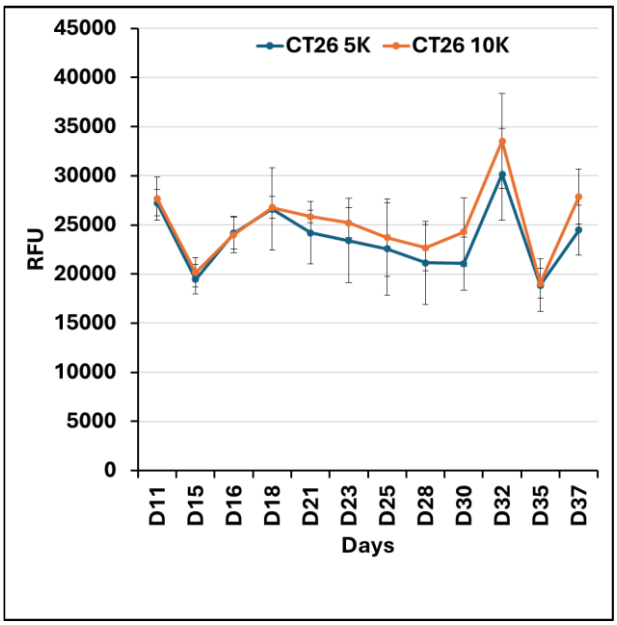

Figure A 3: Relative fluorescence signal as RFU through resazurin cell viability assay of CT26Luc spheroids at different durations of growth, as per the indicated timepoints. N=3 spheroids with one measurement *per spheroid.*

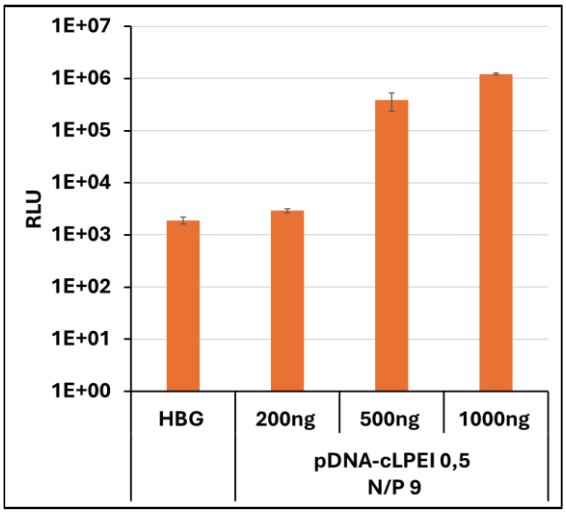

Figure A 4: Gaussia luciferase (GLuc) expression from CT26Luc spheroids (day 20) transfected with Gluc-pDNA based Polyplexes prepared from cLPEI polymers at N/P ratio of 9. Three different concentrations of the Polyplex were utilized for transfection and luminescence is plotted as RLUs. Spheroids treated with HGB buffer were kept as control group. N=2 spheroids with one measurement *per spheroid; 24 h incubation time.*

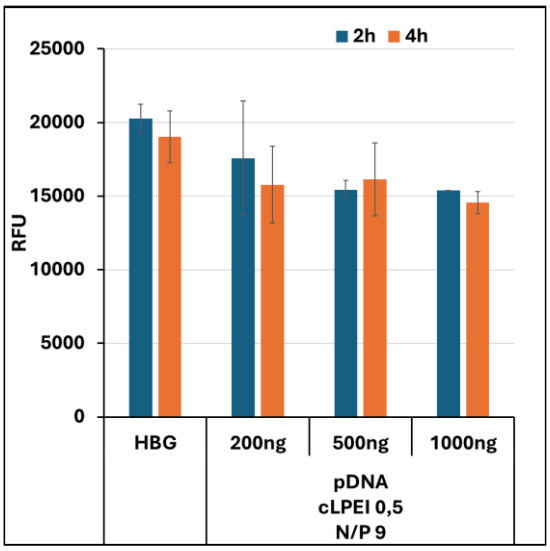

Figure A 5: Relative fluorescence signal as RFU through resazurin assay in CT26Luc spheroids treated with various concentrations of Polyplexes (GLuc-pDNA cLPEI 0,5 N/P 9). The x-axis shows the concentration of the Polyplex formulation. The cell viability difference of initial incubation time of the Polyplexes in basal media (2 h and 4 h) in the spheroids was compared. To assess the cytotoxicity, the control group treated with HBG buffer was included. N=2; readout was done after 24h treatment.

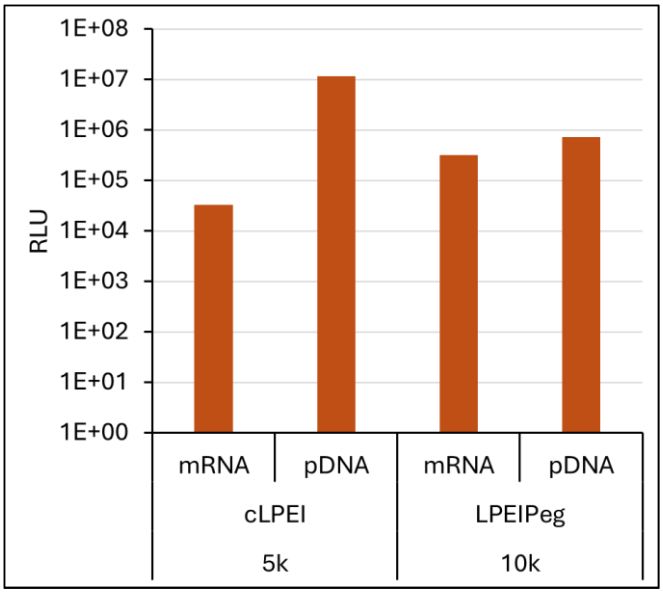

Figure A 6: Gaussia luciferase (GLuc) expression from 5k and 10k 4T1 SCR spheroids (day 20) transfected with GLuc-mRNA and GLuc-pDNA based Polyplexes prepared from LPEIPeg and cLPEI polymers with a N/P ratio of 9. Measured blank media was subtracted and luminescence is plotted as RLUs. N=1 spheroid with one measurement from one spheroid; 24 h incubation time.

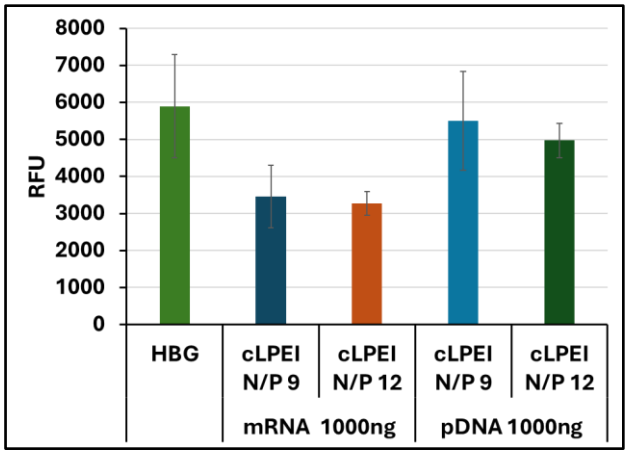

Figure A 7: Relative fluorescence signal as RFU through resazurin cell viability assay on 5k 4T1 SCR (day 8). N=5 spheroids with one measurement per spheroid.

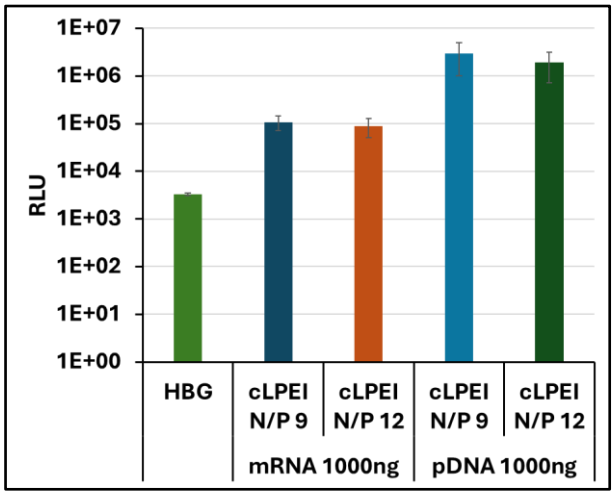

Figure A 8: Gaussia luciferase (GLuc) expression from 4T1 SCR spheroids (day 8) transfected with GLuc-pDNA based and GLuc-mRNA based Polyplexes prepared from cLPEI polymers at N/P ratio of 9 and 12. HBG buffer treated spheroids were kept as a control group. N=5 spheroids with one measurement per spheroid; readout was done after 24 h treatment.

Detailed overviews of the methods and techniques employed per goal

	D0	D1	D2	D3	D4	D5	D6	D7	D8	D9	D10	D11	D12
	seeding	staining optimization	medium change (150µl)		medium change (150µl)			medium change (150µl)		medium change (150µl)		medium change (150µl)	
phase contrast microscopy			X		X			X		X		X	
RSZ Assay			X		X			X		X		X	
necrotic core staining		X	X		X			X		X		X	
formate assay			X		X			X		X		X	

Figure A 9: Overview of the workflow of CT26Luc spheroids with the goal to optimize necrotic core visualization and formate production. Only the first 12 days are shown.

	D0	D1	D2	D3	D4	D5	D6	D7	D8	D9
	seeding		medium change (150µl)			medium change (100µl)	medium change (100µl)			
						oxali added (25, 50, 100, 200µM)	oxali added (25, 50, 100, 200µM)	oxali added (25, 50, 100, 200µM)		
phase contrast microscopy						X	X	X	X	X
RSZ Assay							X	X	X	X
necrotic core staining							X	X	X	X

Figure A 10: Overview of the workflow of CT26Luc spheroids with the goal to assess Oxaliplatin treatment in spheroids on designated timepoints.

	D13	D14	D15	D16	D17	D18	D19	D20	D21	D22	D23	D24	D25
		medium change (150µl)		medium change (150µl), transfection (2h,4h, 6h, 8h, 24h)		medium change (150µl)			medium change (150µl), harvesting, 8 UT & 3 RSZ spheroids left	transfection of 5 spheroids (24h, 72h)	RSZ of the 5 transfected spheroids, harvesting of 3 UT & 3 RSZ spheroids		
phase contrast microscopy		X		X		X			X	X	X		X
RSZ Assay		X		X		X			X		X		X
necrotic core staining		X		X		X			X				
formate assay		X		X		X			X				

Figure A 11: Overview of the workflow of the CT26Luc spheroids with the goal to transfect and evaluate the measured transfection rate. Only day 13 till day 25 are shown. This overview serves as a general overview of how the experiment was conducted.

	D0	D1	D2	D3	D4	D5	D6	D7	D8	D9	D10	D11	D12
	seeding	medium change (150µl)		medium change (150µl)			medium change (150µl)		medium change (150µl)		medium change (150µl)		
phase contrast microscopy		X		X			X		X		X		
RSZ Assay		X		X			X		X		X		
necrotic core staining													
formate assay				X			X		X		X		

Figure A 12: Overview of the workflow of the 4T1 spheroids with the goal to optimize necrotic core visualization and formate production. Only the first 12 days are shown.

	D0	D1	D2	D3	D4	D5	D6	D7	D8	D9	D10	D11	D12
	seeding		medium change (150µl)		medium change (150µl)			medium change (150µl)		medium change (150µl)		medium change (150µl)	
phase contrast microscopy									X	X			
RSZ Assay										X			
Transfection									X				

Figure A 13: Overview of the workflow of the 4T1 SCR spheroids with the goal to transfect and evaluate the measured transfection rate. Only the first 12 days are shown as general experimental design.